JGR Atmospheres

RESEARCH ARTICLE
10.1029/2023JD040396

Special Collection:
Southern Ocean clouds, aerosols, precipitation and radiation

62°S Witnesses the Transition of Boundary Layer Marine Aerosol Pattern Over the Southern Ocean (50°S–68°S, 63°E–150°E) During the Spring and Summer: Results From MARCUS (I)

Qing Niu[1,2], Greg M. McFarquhar[1,2], Roger Marchand[3], Adam Theisen[4], Steven M. Cavallo[1], Connor Flynn[1], Paul J. DeMott[5], Christina S. McCluskey[6], Ruhi S. Humphries[7,8], and Thomas C. J. Hill[5]

[1]School of Meteorology, University of Oklahoma, Norman, OK, USA, [2]Cooperative Institute for Severe and High Impact Weather Research and Operations, Norman, OK, USA, [3]Department of Atmospheric Science, University of Washington, Seattle, WA, USA, [4]Argonne National Laboratory, Lemont, IL, USA, [5]Department of Atmospheric Science, Colorado State University, Fort Collins, CO, USA, [6]Climate Global Dynamics Laboratory, National Center for Atmospheric Research, Boulder, CO, USA, [7]The Commonwealth Scientific and Industrial Research Organisation Environment, Melbourne, ACT, Australia, [8]Australian Antarctic Program Partnership, Institude for Marine and Antarctic Studies, University of Tasmania, Hobart, TAS, Australia

Key Points:

- Machine Learning is applied to identify ship stack contamination of ship-borne aerosol measurements
- Surface Cloud Condensation Nuclei number concentration and its seasonal variation over 62°S–68°S is higher than over 50°S–60°S
- Ice Nucleating Particles over the Southern Ocean originate from primarily organic and biological sources during MARCUS

Supporting Information:

Supporting Information may be found in the online version of this article.

Correspondence to:

Q. Niu,
qingniu@ou.edu

Citation:

Niu, Q., McFarquhar, G. M., Marchand, R., Theisen, A., Cavallo, S. M., Flynn, C., et al. (2024). 62°S witnesses the transition of boundary layer marine aerosol pattern over the Southern Ocean (50°S–68°S, 63°E–150°E) during the spring and summer: Results from MARCUS (I). *Journal of Geophysical Research: Atmospheres*, *129*, e2023JD040396. https://doi.org/10.1029/2023JD040396

Received 10 NOV 2023
Accepted 16 APR 2024

Author Contributions:

Conceptualization: Qing Niu, Greg M. McFarquhar
Data curation: Qing Niu, Thomas C. J. Hill
Formal analysis: Qing Niu, Greg M. McFarquhar
Funding acquisition: Greg M. McFarquhar
Investigation: Qing Niu, Greg M. McFarquhar
Methodology: Qing Niu, Greg M. McFarquhar
Project administration: Greg M. McFarquhar

Abstract The Atmospheric Radiation Measurement Mobile Facility-2 was installed onboard the research vessel Aurora Australis to measure aerosol properties during the 2017–2018 Measurement of Aerosols, Radiation, and CloUds over the pristine Southern ocean (MARCUS) Experiment, providing unique data on aerosols latitudinal and seasonal variation, including south of 60°S where previous observations are scarce. Data from a Cloud Condensation Nuclei (CCN) counter and Ultra-High-Sensitivity Aerosol Spectrometer show that both the number concentration (N_{CCN}) and size distribution of CCN-active aerosols, with diameters (D) between 60 nm < D < 1,000 nm are different over the North Southern Ocean (NSO) (50°S–60°S) and the South Southern Ocean (SSO) (62°S–68°S). The average NSO N_{CCN} at 0.2% and 0.5% supersaturation were 28% and 49% less than that over the SSO. This increase of CCN over the SSO is caused by the increase of aerosols with 60 nm < D < 200 nm, consistent with calculations of Aerosol Scattering Angstrom Exponents derived from a nephelometer. Aerosol hygroscopicity growth factor measured by the Hygroscopic Tandem Differential Mobility Analyzer stayed close to 1.41 for aerosols with 50 nm < D < 250 nm over the SSO, but increased from 1.30 to 1.67 over the NSO, indicating different chemical compositions. Both CCN and Ice Nucleating Particles (INPs) showed a stronger variation with season than with latitude. The variation of heat-labile and presumably proteinacous INPs suggests an increase of ice nucleating-active microbes in summer.

Plain Language Summary The Atmospheric Radiation Measurement Mobile Facility-2 was installed onboard an ice breaker to measure small particles suspended in the air (aerosols), particularly those with potential influences on cloud formation and evolution. The 2017–2018 Measurement of Aerosols, Radiation, and CloUds over the pristine Southern ocean (MARCUS) measurement campaign provides unique data on the latitudinal and seasonal variation of the suspended particles, including south of 60°S where previous observations are scarce. Data show that both the number concentration and size distribution of particles that serve as embryos of cloud droplets are different over the North Southern Ocean (NSO) (50°S–60°S) and the South Southern Ocean (SSO) (62°S–68°S). There are greater concentrations of these embryos over the SSO for increased total amount of suspended particles there. These observations are consistent with data collected by other instruments that show differences over the NSO and SSO in how these suspended particles scatter radiation and how they absorb water vapor, which shows the particles have different sizes and chemical compositions respectively. The concentrations of both particles that serve as embryos for cloud drops and ice crystals both vary more with season than latitude, which has an implication for the energy balance of the Southern Ocean.

1. Introduction

The Southern Ocean (SO), surrounding the ice-covered Antarctic and sea ice, is the most pristine environment on Earth due to its remoteness from anthropogenic and continental aerosol sources (Hamilton et al., 2014; Hoose

Resources: Qing Niu, Greg M. McFarquhar, Adam Theisen, Paul J. DeMott, Christina S. McCluskey
Software: Qing Niu
Supervision: Greg M. McFarquhar, Christina S. McCluskey
Validation: Greg M. McFarquhar
Visualization: Qing Niu, Roger Marchand, Steven M. Cavallo, Connor Flynn
Writing – original draft: Qing Niu, Greg M. McFarquhar
Writing – review & editing: Qing Niu, Greg M. McFarquhar, Roger Marchand, Adam Theisen, Steven M. Cavallo, Connor Flynn, Paul J. DeMott, Christina S. McCluskey, Ruhi S. Humphries, Thomas C. J. Hill

et al., 2009; D. T. McCoy et al., 2015; Uetake et al., 2020) confirmed the pristine nature of the SO boundary layer by documenting the dominance of marine bacteria emitted in sea spray in the marine boundary layer over the SO in a zonal band at latitudes spanning 42.8–66.5°S. Previous studies have also pointed out that aerosols over the SO are primarily natural in origin, including wind-driven primary aerosols such as sea spray, and secondary aerosols such as oxidized products of biogenically produced dimethylsulfide (Quinn et al., 1998). Observations of aerosols in this pristine environment are unique and invaluable for two reasons.

First, the measurements can be used to quantify natural marine aerosols' contribution to direct radiative forcing (Brooks & Thornton, 2018) through scattering, reflection, and absorption of solar radiation as conditions over the SO are as close to pre-industrial as anywhere on Earth. Second, for aerosol-cloud interaction (ACI) research, the measurements can be used to quantify natural aerosols' influence on the formation and evolution of marine boundary cloud properties through their role as Cloud Condensation Nuclei (CCN) or Ice Nucleating Particles (INPs). There is a large bias in shortwave radiation reflected by the cold sectors of extratropical cyclones over the SO in Global Circulation Models (GCMs), such as those involved in the Coupled Model Intercomparison Project —Phase 5 (CMIP5) (Bodas-Salcedo et al., 2014, 2016; Naud et al., 2014), compared to observed radiative fluxes. This bias may be associated with the over-rapid simulated conversion from liquid cloud droplets to ice crystals which decreases the cloud albedo and diminishes the reflected shortwave radiation at the top of atmosphere (Bodas-Salcedo et al., 2014; D'Alessandro et al., 2021; Flato et al., 2013). Although more recent model simulations have reduced this particular bias, the bias is still prominent over the SO close to the Antarctic coast (Gettelman et al., 2020; Zhou et al., 2021). Satellite retrievals over the SO highlight the natural marine cloud brightening over the Antarctic marginalized sea ice area (Mace et al., 2023). However, this has not been captured by the CMIP6 models yet (Mallet et al., 2023), and essentially the modeled clouds south of 60°S are still not bright enough.

Prior satellite retrievals over the SO (Huang, Siems, Manton, Hande, & Haynes, 2012; Huang, Siems, Manton, Protat, & Delanoë, 2012) have acknowledged the importance of supercooled liquid water (SLW), which may at times be more prevalent over the SO than at equivalent latitudes and temperatures in the Northern Hemisphere (Huang et al., 2015; Y. Hu et al., 2010; McFarquhar et al., 2021). Because the scattering and absorption properties of liquid and ice differ (Sun & Shine, 1994) and because many parameterizations in models are based on observations collected in the more polluted and land-based Northern Hemisphere that lead to more efficient ice nucleation and cloud glaciation (Burrows et al., 2013), global model biases occur, and tend to increase with latitude (Bodas-Salcedo et al., 2014, 2016).

Updates to GCMs to reflect an enhanced understanding of cloud and aerosol processes have improved the representation of the radiative budget north of 60°S; however, the discrepancies south of 60°S are compounded by the fact that there are very limited air-borne aerosol and cloud measurements over the Antarctic marginalized sea ice area. The reasons behind the models' inability to capture natural marine cloud brightening are still unknown. To improve cloud representation over the SO, particularly the Antarctic sea ice marginal zone, more and higher quality observations of clouds and aerosols over the SO, and the potential physical justification for more frequent SLW over the SO, are needed.

The microphysical properties of low clouds, such as the concentration of cloud droplets, which influence cloud reflectance, are sensitive to the concentrations of CCN. Therefore understanding the sources and sinks of CCN is crucial to understanding SO clouds (Kang et al., 2021). Over the remote SO in the Marine Boundary Layer (MBL), natural aerosols, especially those in the accumulation mode (Ac, aerosols with diameter (D) between 60 and 1,000 nm), have long residence times of 1–5 days in the boundary layer, 5–10 days between 4 and 8 km, and a few weeks between 8 and 13 km, because they do not sediment quickly nor coagulate easily (Williams et al., 2002). They are capable of serving as CCN as they are large enough to nucleate at typical supersaturations in the atmosphere. Recent in situ observations in the region suggests that 0.3% is a typical in-cloud supersaturation found in stratocumuli clouds (Fossum et al., 2018; Sanchez et al., 2021; Twohy et al., 2021). Wet scavenging can be a main sink for Ac, and precipitation intensity together with duration can affect the amount of Ac.

Extratropical cyclones are pervasive over the SO (Hoskins & Hodges, 2005; Lang et al., 2018; Simmonds & Keay, 2000) and are accompanied by substantial cloud cover, particularly by low clouds below 3 km altitude and boundary layer precipitation (IPCC, 2013; Mace, 2010; D. T. McCoy et al., 2014). This makes the SO an ideal natural laboratory for aerosol-cloud-interaction studies. However, the remote and synoptically active environment of the SO increases the logistical challenges of deploying instruments to measure aerosols, CCN and INPs.

Therefore few comprehensive aerosol, cloud, and meteorology focused field campaigns have been conducted in this region, especially south of 60°S, until recently. Recent experiments include the Measurements of Aerosols, Radiation and CloUds over the Southern Ocean (MARCUS), the Clouds, Aerosols, Precipitation, Radiation, and atmospherIc Composition Over the southeRn oceaN (CAPRICORN), the Southern Ocean Clouds, Radiation, Aerosol Transport Experimental Study (SOCRATES), and the Antarctic Circumnavigation Expedition (ACE), which made observations of aerosols, clouds, and precipitation over the SO (McFarquhar et al., 2021; Schmale et al., 2019). In particular, MARCUS, conducted in spring and summer of 2017–2018 made observations of the seasonal variation of aerosol properties at high latitudes over the Australasia sector of the SO. In this study, MARCUS observations acquired by instruments installed on the icebreaker RSV Aurora Australis, which traversed back and forth between Hobart, Australia and the Australian East Antarctic stations in the 2017–2018 period, are analyzed.

Xi et al. (2022) examined how cloud properties varied by latitude with a demarcation line of 60°S, noting higher total cloud fractions (90.3%), lower cloud liquid water paths, lower precipitable water, and more mixed-phase clouds south of 60°S compared to north of 60°S. This discernible shift of cloud properties can be related to the variation of aerosols over different regions. Humphries et al. (2021) also examined the latitudinal gradient of aerosol concentrations, specifically those of CCN, but did not examine the latitudinal dependence of accumulation-mode-aerosol size distributions or aerosol optical and hygroscopic properties. Twohy et al. (2021) used a combination of SOCRATES and CAPRICORN data to examine the sub-micron aerosol composition between Tasmania and 65.7°S and CCN species north of 62°S, showing an increase of sulfate and methanesulfonic acid (MSA) concentrations south of 62°S compared to further north.

Other recent studies have examined the influence of Recent Particle Formation (RPF) on the marine aerosol variability and low cloud properties over the remote ocean. For example, I. McCoy et al. (2020) showed the SO free troposphere (3–6 km) is characterized by widespread, frequent RPF events contributing to Aitken-mode aerosol particle (0.01–0.1 μm) concentrations, which subside into the boundary layer and grow into accumulation mode aerosols. However, I. McCoy et al. (2020) only examined airborne observations of Ac below, above and within the clouds, and did not analyze the surface aerosol conditions which is close to important sources of primary aerosols.

However, there are limited studies that focus on the distribution of aerosols close to the Antarctic coast thus preventing the analysis of (a) how cloud properties vary in the context of varying aerosol loading, and (b) how cloud properties influence boundary layer aerosols over the SSO. MARCUS had more shipborne data collected over the SSO compared to CAPRICORN, enabling this study extend previous studies conducted over the SO by providing information about both the seasonality and latitude variation of marine boundary layer CCN-active and INP-active aerosols over the SSO where analyses have previously been limited. This study also aims at comparing the properties of CCN and INP between the SSO and NSO, which may be related to the change of clouds shown in Xi et al. (2022).

The remainder of the study is organized as follows. Section 2 introduces the MARCUS data and quality control procedures, including the development of a new methodology for removing aerosol data contaminated by the Aurora Australis ship stack. Section 3 presents observations of accumulation mode aerosols, CCN, aerosol optical properties and hygroscopicity over the NSO and SSO by season and latitude. Section 4 shows the INP latitudinal and seasonal variation. Section 5 summarizes the main findings and potential directions for future research.

2. Methodology and Data

2.1. Voyage Overview

During MARCUS, the AA made three full latitudinal transects of the SO on resupply voyages from Hobart, Australia (42.9°S, 147.3°E) to the Australian Antarctic stations Casey (66.16°S, 110.3°E), Davis (68.3°S, 77.6°E), and Mawson (67.4°S, 62.5°E). The AA also made one voyage to the Macquarie Island research station (54.4°S, 158.5°E). Overall data were collected from 29 October 2017 to 24 March 2018 (Figure 1). This 144-day period included the Austral spring and summer. The nature of the resupply voyages means that specific cloud or weather systems were not targeted.

The transit time, across the SO and through the sea ice, from Hobart to Antarctica was approximately 2 weeks, with the AA spending 1–2 weeks moored at a station during the resupply. Data from the aerosol probes while the

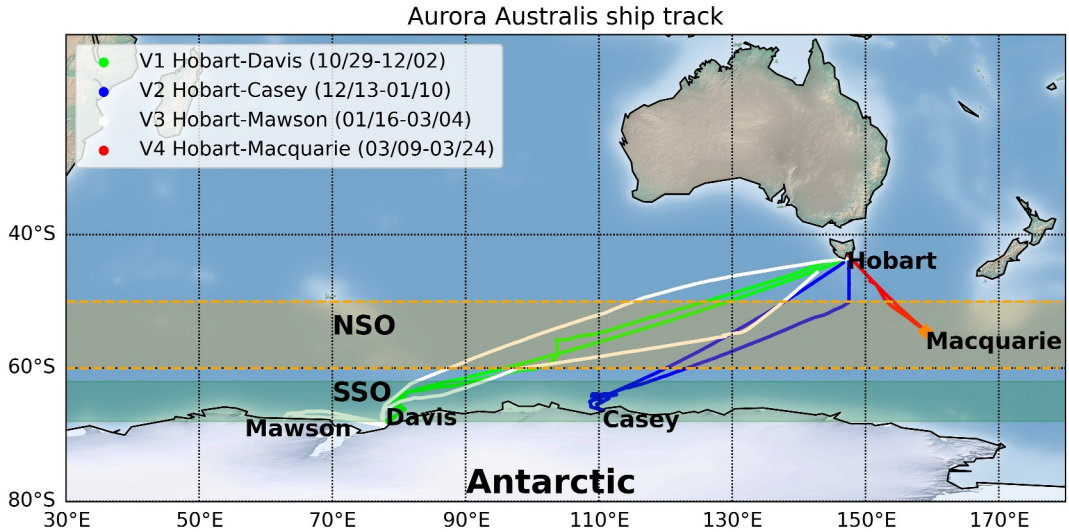

Figure 1. Ship tracks during MARCUS with voyage illustrated by color shown in legend. The orange and green shaded area represent the north Southern Ocean (NSO) and south Southern Ocean (SSO) respectively.

AA was in port were not used for analysis to avoid contamination from anthropogenic pollutants from the Antarctic stations. The measurements of INP used in this study do include some in-port time period considering the sample window is 23–48hr. McFarquhar et al. (2021) provide more details on the meteorological systems sampled during MARCUS, the instruments installed on the AA, and the context of the MARCUS data in terms of other projects conducted during a similar time period over the SO.

2.2. Instrumentation

McFarquhar et al. (2021) review the instrumentation installed on the AA to measure clouds, aerosols, radiative and precipitation properties during MARCUS. In this section, a review of only the aerosol, CCN, and INP instrumentation used in this study (Table 2) are provided together with a description of the processing procedures.

The primary measurements of aerosols were acquired with instruments included in the second ARM Mobile Facility 2 (AMF2) Aerosol Observing System (AOS) (Uin & Smith, 2020; Uin et al., 2019). The AMF2 AOS includes a suite of instruments in a container that was located at the top of a wheelhouse (approximately 24 m above sea level) on the bridge deck of the AA. The AOS inlet was covered by a stainless-steel rain shield with a meteorological station mounted on the shield top. The exact location of the instruments on the *AA* can be found in the Appendix of Humphries et al. (2021).

The TSI Model 3772 Condensation Particle Counter (CPC) was used to detect the concentration of total Condensation Nuclei (CN), aerosols with 10 nm < D < 3 μm, over a concentration range from 0 to 10^4 cm^{-3} (Koontz, Kuang, et al., 2018). The CPC condenses and grows particles to super-micron sizes and then counts them individually with an Optical Particle Counter. Unlike measurements made at a fixed site where uncertainty is dominated by statistical errors in the single particle-counting mode, the inlet flow rate typically has a variability of up to 5% for measurements made on a vessel, which primarily contributes to the measurement uncertainty (Kuang, 2016a, 2016b).

The Ultra-High Sensitive Aerosol Spectrometer (UHSAS) manufactured by Droplet Measurement Technologies, Inc. provides aerosol size distributions for particles with 60 nm < D < 1,000 nm (Uin, Senum, et al., 2018). Data were processed with a time resolution of 10 s. The light scattered by particles passing through an infrared laser (1,054 nm) was measured by optical detectors to determine D. The first five bins (D < 70 nm) were not used since the data do not have high quality (Janek Uin, personal communication, 28 March 2024). There was a stable sample flow of around 50 cm^{-3} min^{-1} through the UHSAS during MARCUS, indicating concentrations in the range of 0–3,600 cm^{-3} could be detected. The manufacturer specifies the uncertainty of particle sizing as 2.5% in the laboratory but higher on-site (Uin, 2016c).

The Cloud Condensation Nuclei Counter (CCN-100) manufactured by Droplet Measurement Technologies Inc. measures the concentration of CCN as a function of supersaturation in the humidifier (Uin, Andrews, et al., 2018). The CCN-100 draws a volume of air into one column chamber with an adjustable supersaturation, where an OPC is used to size and count the particles. For MARCUS, an hourly cycle was adopted such that the Supersaturation (*SS*) was changed every 12 min, providing 10 min of observations and 2 min of equilibration at each change. The *SS* chosen (in order) were 0.1%, 0.2%, 0.5%, 0.8%, and 1.0% to include the range of typical SS over the SO. The whole cycle normally lasted for 1 hr and therefore the concentration of CCN at each SS hourly is available. Uncertainty of single particle counting depends on the total aerosol particle concentration and is less than 4% in ideal conditions but higher on site (details in Table 2) (Uin, 2016a).

Number concentrations of immersion freezing INPs (N_{INP}) were measured during MARCUS with the Colorado State University (CSU) ice spectrometer (DeMott et al., 2018). Composite INP concentrations versus temperature from MARCUS have been presented in Raman et al. (2023), but additional investigations of latitudinal distribution and inferences to INP types are made herein. An open faced poly-carbonate filter (0.2 micron pore size), sited approximately 18 m above the ocean surface, was used to collect suspended ambient particles of all sizes (McCluskey, Hill, Sultana, et al., 2018). Filters were stored frozen until removal of particles into suspensions in pure water for offline treatment to identify INP type. Measurements were considered below the detection limit if the INP number concentration or the 95% confidence interval extended below zero. Two treatments were conducted on aerosol samples to determine the contributions of heat-labile and organic material fraction respectively. A detailed description of these 95°C heating and hydrogen peroxide (H_2O_2) digestion methods are included in McCluskey, Hill, Sultana, et al. (2018).

The TSI model 3563 Integrating Nephelometer instrument measures aerosol light scattering as a function of wavelength (Koontz, Flynn, et al., 2018; Uin, Salwen, et al., 2018). The main observables include the aerosol particle optical scattering coefficients (total scatter and backscatter) for three wavelengths (700, 550, and 450 nm). It had two impactors installed, one to only sample aerosols with D < 1 μm (PM_1) and the other that limit aerosols with D < 10 μm (PM_{10}). Based on modeling and experimental results the systematic uncertainty in ideal conditions is estimated to be within 10% (Uin, 2016b). With the same wavelengths and filters, the Particle Soot Absorption Photometer (PSAP) collects aerosol particles on a substrate and measures the change in light transmission relative to a reference filter, which thus provides aerosol absorbing properties.

The Humidified Tandem Differential Mobility Analyzer (HTDMA) 3100 manufactured by Brechtel Manufacturing, Inc. measures aerosol particle growth factor due to water uptake (Uin, Cromwel, et al., 2018). The first differential mobility analyzer (DMA) selected a narrow size range of dry aerosol particles (from 50 to 250 nm in 50 nm steps), which were exposed to 80% RH. The second DMA and a CPC were used to measure the resulting size distributions. From the initial dry particle size and the size distribution of the humidified particles, a growth factor was derived. Particle sizing uncertainty is less than approximately 5% in the laboratory but higher in the field (Uin, 2016d). The HTDMA data quality periodically are affected due to one or more following reasons: external dry air supply not working, sample contaminated by ship's exhaust, and troubleshooting internal instrument issues (low RH, unstable power).

For the above aerosol instruments, the CPC, UHSAS, and HTDMA sampled air after drying with a nafion dryer, however, the CCN-100, nephelometer.

2.3. Machine Learning Algorithm

Gras (1995) previously found the average CN concentration (N_{CN}) during summertime over the SO was 89.5 cm^{-3}. However, the MARCUS CPC measured frequent and intense CN spikes with concentrations orders of magnitude larger than observations acquired in close proximity. Furthermore, 71% of observation periods with CN larger than 2,000 cm^{-3} during MARCUS were associated with a CO mixing ratio higher than 0.08 ppmv. This suggests that the spikes in N_{CN} are caused by contamination from the ship stack when hydrocarbon fuels are burned and a range of combustion products, including CO_2, water vapor, nitrogen oxides (NO_x), sulfur dioxide (SO_2), carbon monoxide (CO) and particulate matter, including black carbon (BC), etc. (Assessment, 2009; Turner et al., 2017) are emitted through the chimney. Because ship-stack exhaust contaminated a large fraction of the aerosol measurements during MARCUS, including measurements of Cloud Condensation Nuclei (CCN), it is important to isolate time periods contaminated by effluents from the ship stack before analyzing latitudinal and seasonal trends in aerosol quantities.

Humphries et al. (2019) developed an algorithm applying the median absolute deviation (MAD) to detect observation value outliers for the Australian blue-water Research Vessel (RV) Investigator. However, eliminating time periods with ship-stack contamination without eliminating periods when aerosol probes measured enhanced concentrations of background aerosols is challenging because peaks and dips in N_{CN} can also be associated with natural effects such as the presence of plankton blooms and wet scavenging, as well as ship stack contamination. In addition, the different ship fuel grade, engine power, as well as the location of aerosol probe inlet. also affect the products and processes of combustion through the chemical reactions happening in and near the chimney when the exhaust blends with local air masses over the monkey deck (Sinha et al., 2003).

An algorithm was thus developed using a supervised machine learning (ML) model to identify time periods when the MARCUS aerosol measurements in Table 2 were contaminated and unperturbed by the ship stack in a three-step process: (a) customizing the embedded Quality Control (QC) flags produced during the ARM standard ingest processes for the ML input features, CO and O_3 data, (b) prediction by a ML model, and (c) transferring ML predictability as ML flags and applying to measurements made with the UHSAS, CCN, CPC, HTDMA, PSAP, nephelometer, applying original embedded data QC flags, and manual screening.

First, the input data for the ML algorithm uses only data that have passed the ARM data embedded QC in a customized process. In particular, the QC office flagged data with labels such as "calibration mode," "missing values," "warning larger than the maximum value," "invalid larger than the maximum value," etc. While data obtained during calibrations and missing data cannot be input to the ML model, data identified by the ARM QC process as larger than the "maximum warning value" and "maximum valid value" are included because they may or may not be caused by ship-stack contamination.

Second, data acquired from 11 to 14 November 2017 are manually labeled as time periods with or without ship stack contamination. By order, the PM_1 (particles with $D < 1$ μm) absorption coefficient (B_a), the total aerosol number concentration (N_{CN}) measured by the CPC, and the size distribution of accumulation mode aerosol particles acquired from the UHSAS are referred to and used for the manual label. B_a is evaluated first since it emphasizes the existence of black carbon, which is a great tracer for ship stacks in this pristine environment. CN is then examined as the most sensitive variable to identify ship stack contamination in the AOS for its high sampling frequency (1 Hz) and instant response to ship stack contaminants. Ac data (0.1 Hz) are then used for cross-checking. Figure 2 shows the result of this manual labeling. Contaminated periods have an instantaneous and drastic increase in CN and Ac as shown by the red dots and the brighter stripe in Figure 2a, a drastic increase in CO as shown in Figure 2c, a decrease in O_3 as shown in Figure 2d, and values of $B_s > 0.9\ \mathrm{Mm}^{-1}$ and $B_a > 0.4\ \mathrm{Mm}^{-1}$ as shown in Figure 2b with red coloring indicating ship-stack contamination periods.

Thereafter, the CO and O_3 data acquired from 13 to 14 November 2017 that went through the first and second steps together with their manual labels are used as training data for a supervised Random Forest algorithm (Pedregosa et al., 2011), and the data acquired from 11 to 12 November 2017 are used for ML model validation. The Grid-Search method is used in searching for a reasonable hyper-parameter for the ML model, with 5 used as the total number of trees, 5 as the depth of branches, and 2 as the minimum number of leaves with no random-state. The time periods where O_3 and CO were identified as contaminated/unperturbed by the ML method were compared against those from the manual identification of the aerosol quantities at 1 Hz frequency as shown in Figure 2. A validation score F1 is computed as

$$F1 = TP/(TP + 1/2(FP + FN)), \quad (1)$$

where FP is defined as the number of False-Positive events, TP as True-Positive and FN as False-Negative (Fawcett, 2006). The F1 score for 11–12 November 2017 is 93%. The FP events that prevented a perfect ML algorithm are caused by the CO spikes on 12 November at 00Z and on 11 November at 06Z. They are manually labeled as "unperturbed" in Figures 2b–2d, but the ML model predicts them as contaminated in Figure 2a because of the increased CO.

In general, the CO measured down-flow of the ship stack is substantially higher than in uncontaminated regions due to insufficient combustion. This is seen on 12 November in Figure 2c, compared to the atmosphere unperturbed by flow from the stack for most of 11 November. The chimney also serves as a local point source of NO_x, which in the immediate vicinity of the chimney depresses O_3 through NO_x titration which occurs on a time period

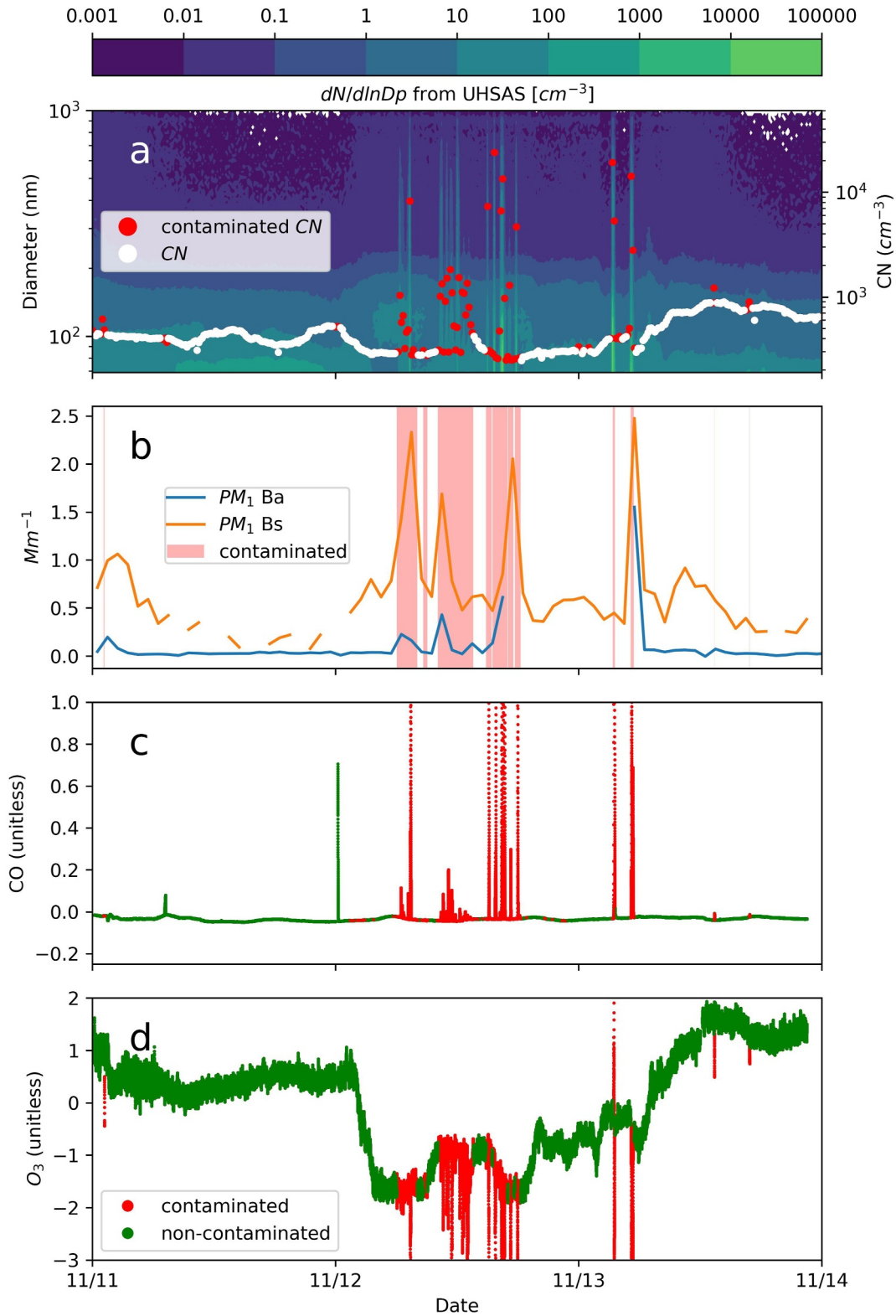

Figure 2.

of seconds. This NO_x titration process was previously successfully captured by laboratory experiments and simulated in climate models (X.-M. Hu et al., 2019; Tang et al., 2021). Using O_3 as reference for the ship stack was also used by Humphries et al. (2015) in previous aerosol measurements on *AA*.

The ML model was applied to all the other MARCUS data for times when the ship was out-of-port. An example of its application is seen in Figure 3 and in Figures S1–S8 of the Supporting Information S1. Each voyage is plotted separately and there are no manual screening results included in this step in order to better visualize the ML model performance. The ML model provides a ship-stack probability as output, a probability close to one implies very possible ship-stack contamination, and close to zero implies likely unperturbed by the stack.

For each voyage, the 1 Hz ML predicted probability are transferred into a ML flag for each 10-min time window based on the values and frequencies of the probability during the 10-min. The thresholds used for probability are different, potentially influenced by the different wind direction relative to the ship motion. The mean probabilities are calculated accordingly, and the ML flag is set as contaminated when its mean probability is larger than a threshold. The thresholds here range from 0.001 (between Hobart and Mawson) to 0.01 (between Hobart and Davis), and to define the acceptable range deserves thoughtful subjective consideration. The ML model output is applied to all aerosol variables listed in Table 1 so that all aerosol data for periods identified as contaminated are removed from the analysis.

The final step combines application of the ARM QC flags of each variable together with the ML flag to ensure all data used in the analysis are both unperturbed and are acquired when instruments operate normally. To clarify the difference from the first step, QC flags are previously only used to indicate the instruments' operation status, with the thresholds (warning values, invalid values) designed to test the measurements ignored so that the ML has informative CO and O_3 mixing ratio as input. In the final step, the original ARM QC thresholds and ML flags are both applied before the manual screening. The manual screening contains objective input such as B_a and the aerosol concentrations from the HTDMA using a dry diameter of 50 nm. It also contains subjective inputs. For example, considering the time resolution of the CPC, CCN-100, and nephelometer are different, when CN measured from the CPC shows the peaks signals are caused by the ship stack according to the ML flags or ARM QC flags, the extent to which the hourly N_{CCN} should be labeled as unperturbed needs manual subjective decision.

To evaluate the ML methodology, the time periods identified as contaminated were compared against those identified by Humphries et al. (2021) for MARCUS. Humphries et al. (2021) used peaks of total aerosol number and CO concentration to identify periods of ship stack contamination and removed more than 90% of the aerosol observations from the MARCUS data set. Although increases of aerosol concentrations frequently occurred in contaminated periods, avoiding the use of aerosol concentration to identify time periods of exhaust better allows the time periods of enhanced aerosol concentration due to natural variability to be included in the accepted data. Although each transit is contaminated to a different extent, overall the ML model identifies 68% of times as influenced by the ship stack. Conclusions derived using both methods about latitudinal trend are consistent. More details about the application of the ML algorithm to different time periods are found in Supporting Information S1.

2.4. Derived Aerosol Optical Property: Angstrom Exponent

An aerosol optical property, the Angstrom Exponent, derived using the MARCUS data was examined to determine if the latitudinal trends in optical properties were consistent with those of aerosol size. Ångström (1929) first noted the spectral dependence of extinction by particles may be approximated as a power law relationship given by

Figure 2. Time series of (a) size distributions measured by UHSAS with total CN measured by CPC superimposed, (b) PM_1 total scattering coefficient (B_s) and absorbing coefficient (B_a) derived from PSAP, (c) unitless CO mixing ratio, and (d) unitless O_3 concentration. The green colors in (c) and (d) indicate times identified as uncontaminated by ship stack as determined from manual identification of aerosol data in (a) and (b), whereas red color or shading in (b)–(d) indicate time periods manually labeled as ship stack contaminated. The red color in (a) indicates the ML predicted contaminated times for validation and training data set. Both CO and O_3 shown have been scaled so that the mean is removed, and values are scaled to unit variance.

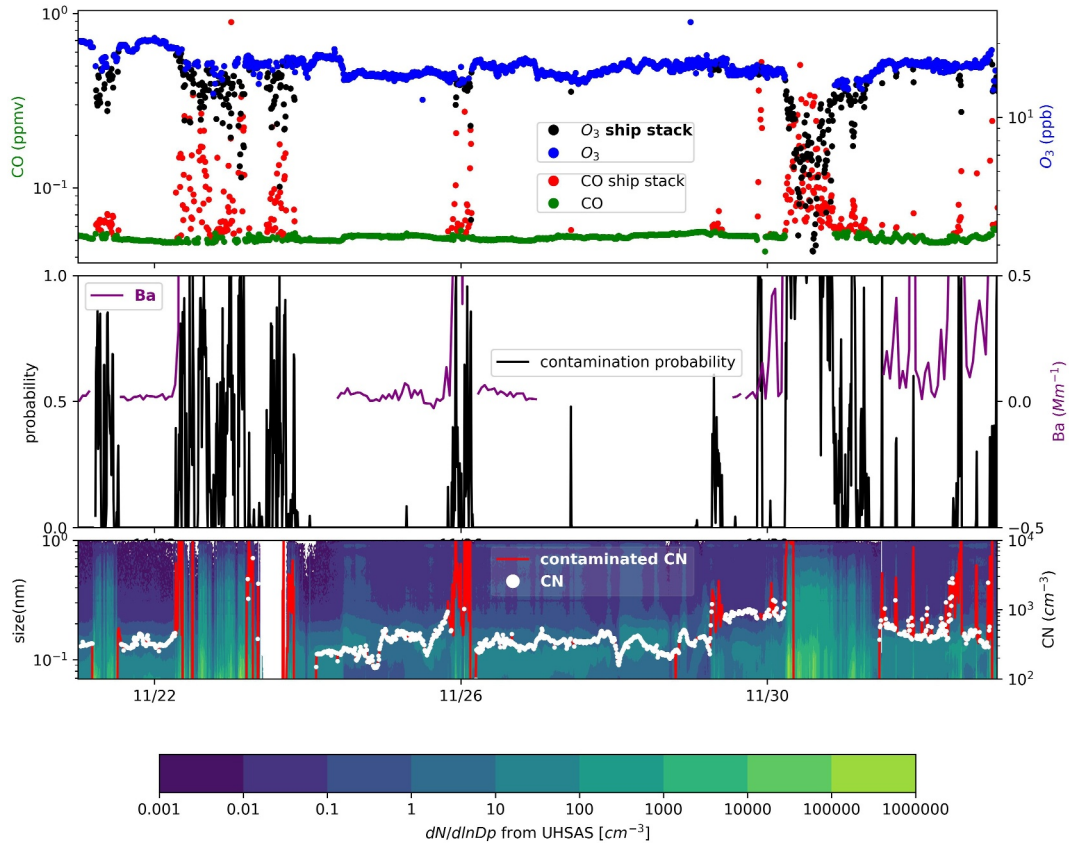

Figure 3. Random Forest model applied to time series of (a) CO mixing ratio and O_3 concentration; (b) PM1 total absorbing coefficient (B_a) derived from PSAP in purple and the ML predicted contamination probability in black; (c) size distribution measured by UHSAS with CN measured by CPC superimposed. The green and blue colors in (a) indicate times identified as uncontaminated by ship stack as determined by contamination probability in (b).

$$AOD(\lambda) = \beta\left(\frac{\lambda}{\lambda_0}\right)^{-\alpha}, \tag{2}$$

where λ_0 equals to 1 μm, λ is the wavelength, AOD is the aerosol optical depth at that wavelength, α is the unitless Angstrom Exponent (AE) and β is Angstrom's turbidity coefficient which equals AOD at $\lambda = 1$ μm. Thus, α is a qualitative indicator of the wavelength dependence of AOD, which gives basic information on the aerosol size distribution. While the AOD is broadly used in vertical-oriented satellite retrievals, aerosol probes measure bulk properties such as total scattering and total absorption coefficients instead. In the equations below, the AE is denoted α.

The ship-borne nephelometer and PSAP measure the total scattering coefficient (B_s) and total absorption coefficient, which are, respectively, used to derive the scattering Angstrom Exponent (α) and absorption Angstrom Exponent. The scattering α is more dependent on the aerosol size, while the absorbing α more strongly depends on the aerosol type and chemical composition (Ångström, 1929; Kaufman, 1993; Schuster et al., 2006).

Computing the logarithm of the ratio of AOD at two different wavelengths using Equation 2 (the subscripts 1 and 2 refer to these wavelengths) allows the Angstrom wavelength exponent to be computed from the spectral values of B_s as given by

$$\alpha = -\frac{dlnBs}{dln\lambda} = -\frac{\ln(Bs_2/Bs_1)}{\ln(\lambda_2/\lambda_1)}. \tag{3}$$

Journal of Geophysical Research: Atmospheres

10.1029/2023JD040396

Table 1
MARCUS Aerosol and INP Measurements Used in This Study

Variable	Description	Instrument	Range	Sampling frequency	Uncertainty
N_{CN}	Total aerosol number concentration	CPC	10 nm^{-3} μm	1 Hz, 10 min mean applied	<10% (if N_{CN} < 10,000 cm^{-3})
N_{Ac}	Number concentration of accumulation mode aerosol	UHSAS	0.06–1.0 μm	0.1 Hz, 10 min mean applied	5%–10% (during high counting efficiency)
N_{CCN}	Number concentration of CCN	CCN-100	SS at 0.1%, 0.2%, 0.5%, 0.8%, 1.0%	1 Hz (alternate every 12-min for each SS, thus hourly $N_{CCN,SS}$)	5% for sample flow, higher for supersaturation set point
N_{INP}	Number concentration of INP	Ice Spectrometer	Total suspended aerosol	23–51 hr	Depends on detection limit and smoke contamination
B_s	Total aerosol light scattering coefficient	Nephelometer	PM_{10} or PM_1	1 Hz, 10 min mean applied	<5% based on span check
B_a	Total aerosol light absorbing coefficient	PSAP	PM_{10} or PM_1	10 min mean applied	up to 50%
HGF	Hygroscopicity growth factor, unitless	HTDMA	*D* of 100, 150, 200, 250 nm	10 min mean applied	4% for RH, 10 nm for sizing accuracy

Note. PM_1 includes aerosols with D < 1 μm, and PM_{10}, aerosols with D < 10 μm. The uncertainties reported above are acquired from instrument mentors (personal communication) and handbooks, and apply when instruments are calibrated in laboratories. The uncertainties in MARCUS can be influenced by conditions such as air pressure, air flow, sea spray contamination, high particles number concentration during plumes, and therefore may be higher than the numbers in this table.

Table 2
Defined Variables With Acronym

Variable	Acronym
Ac	Accumulation Mode Aerosol
CN	total Condensation Nuclei
CCN	Cloud Condensation Nuclei
CPC	Condensation Particle Counter
DMA	Differential Mobility Analyzer
FBAP	Fluorescent Biological Aerosol Particle
HGF	Hygroscopic Growth Factor
HTDMA	Humidified Tandem Differential Mobility Analyzer
INP	Ice Nucleating Particle
MSA	Methanesulfonic-acid
NSO	North Southern Ocean
RPF	Recent Particle Formation
SSO	South Southern Ocean
UHSAS	Ultra High Sensitivity Aerosol Spectrometer

While B_s indicates aerosol loading, the spectral variability of B_s contains information about the aerosol size distributions and the average radius. α close to 4 represents Rayleigh scattering where particles are small compared to the wavelength, which is the case for visible light. α close to zero or slightly negative represents geometric optics where particles are large compared to the wavelength (λ), such as for cloud droplets with D > 5 μm and visible light.

3. Latitudinal and Seasonal Variation of CCN-Active Aerosols

3.1. Cloud Condensation Nuclei

Recent aircraft-based cloud droplet number and below cloud CCN measurements over the Australasian sector of the SO suggest that the typical maximum supersaturation reached in clouds over the SO is about 0.3% (Sanchez et al., 2021; Twohy et al., 2021). Therefore, analysis of the latitudinal and seasonal dependence of CCN in this study concentrates on measurements made at SS of 0.2% and 0.5%.

MARCUS mostly covers the months of (in order) November, December, January, and February. The cruise between Hobart and Macquarie Island does not include the SSO region and therefore is excluded from the analysis presented in Figures 4 and 5. Based on the 2017–2018 sea surface temperature (SST) record, the hottest and coldest month is February and November within the observation period respectively, with January warmer than December. Therefore November combined with December are viewed as spring months for this region, and February combined with January are identified as summer months in subsequent analysis in this study.

Figure 4a shows the latitudinal distribution of CCN concentration (N_{CCN}) at 0.2% ($N_{CCN,0.2}$) and 0.5% SS ($N_{CCN,0.5}$) using data from the first three voyages during MARCUS after the removal of observations contaminated by the ship stack. The 1° bin is chosen based on the statistics required for reasonable interpretation of the data as latitudinally driven instead of synoptically driven. As the latitude changes from 50°S to near the Antarctic coast (67°S), $N_{CCN,0.2}$ and $N_{CCN,0.5}$ share a similar spatial pattern, with their median values staying low between 50°S and 62°S (NSO) and then increasing south of 62°S (SSO). The boundaries of the NSO and SSO were chosen based on data significance tests that gave the maximum difference between the NSO and SSO. The boundary latitude may have a seasonality and the choice of 62°S is consistent with previous observations and modeling (Humphries et al., 2021). The increased N_{CCN} over the SSO can be related to the higher cloud fraction reported in Xi et al. (2022) and the higher cloud droplet concentration reported in Mace et al. (2023) in this region. Models struggle to represent cloud characteristics in the vicinity of the Antarctic peninsula (Mallet et al., 2023), and it is speculated that this may be related to difficulties in representing CCN and aerosols.

$N_{CCN,0.2}$ ($N_{CCN,0.5}$) varied over the NSO from 59 to 86 cm^{-3} with a mean of 71.4 cm^{-3} (79–140 cm^{-3} and mean of 98.5 cm^{-3}), with a local minimum around 57°S. Over the SSO, the $N_{CCN,0.2}$ ($N_{CCN,0.5}$) generally increased from 60 cm^{-3} (79 cm^{-3}) at 62°S to 118 cm^{-3} (238 cm^{-3}) near the Antarctic coast, with a local maximum of 171 cm^{-3} (310 cm^{-3}) around 65°S. The location of this maximum is consistently at 64°S in both spring and summer, as shown in Figures 4b and 4d, respectively. However, there are differences in the mean and ranges of $N_{CCN,0.2}$ and $N_{CCN,0.5}$ in spring and summer.

In spring (Figure 4b), $N_{CCN,0.2}$ and $N_{CCN,0.5}$ have persistent and similar low variability, with higher variations over the SSO than over the NSO. Variations over both the NSO and SSO are larger in summer than in spring. This is likely caused by the stronger sources and sinks in the summer, such as an intense phytoplankton bloom and wet scavenging. Therefore, with a comparable number of samples in summer and spring, as indicated in Figures 4c and 4e, for the seasons combined in Figure 3a, the latitudinal variability over the NSO in $N_{CCN,0.2}$ and $N_{CCN,0.5}$ is dominated by contributions from the summer. The black lines in all figures show the number concentration of Ac (N_{Ac}), which is usually between $N_{CCN,0.2}$ and $N_{CCN,0.5}$, but typically closer to $N_{CCN,0.2}$. This gives an indication of aerosol concentrations over size ranges for particles that typically act as CCN. However, there are latitudes, such

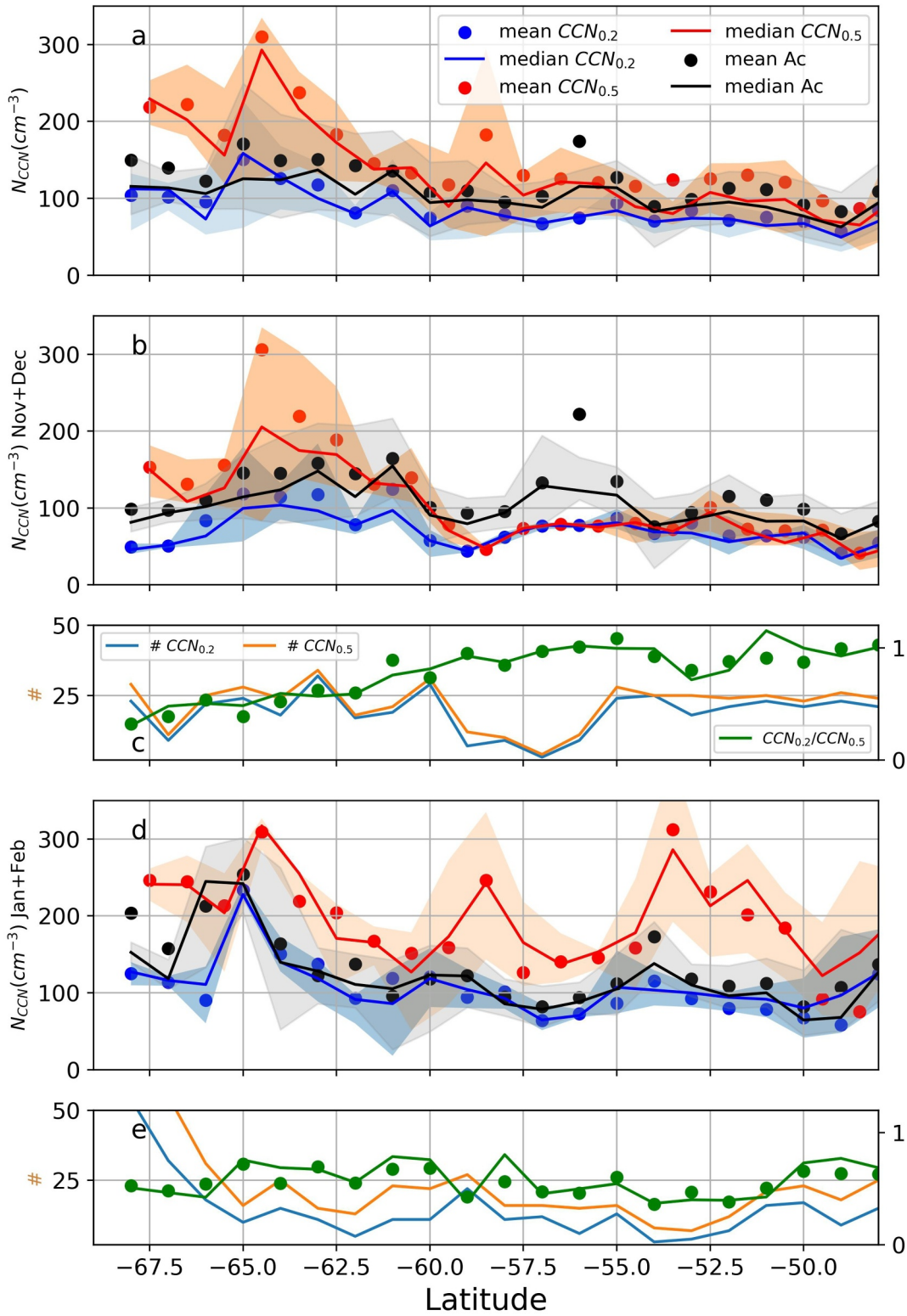

Figure 4.

as north of 60°S during the spring, where the Ac line is higher than both the $N_{CCN,0.2}$ and $N_{CCN,0.5}$, showing that not all accumulation mode aerosols act as CCN even at 0.5% supersaturation.

While Ac is counted based on particle sizes, the ambient supersaturation and aerosol chemical composition determine whether an aerosol actually serves as a CCN. In Figure 4b, over the NSO, N_{Ac} is higher than $N_{CCN,0.5}$, indicating some Ac are not good CCN even at 0.5% SS. On the other hand, over the SSO, N_{Ac} is higher than $N_{CCN,0.2}$ but lower than $N_{CCN,0.5}$. This means that over the spring SSO, 0.2% SS can activate a significant fraction of Ac present, but also that there is a larger pool of particles (below the 60 nm threshold used by the UHSAS) that will activate at 0.5% SS. Further experiments should measure and provide more information about aerosol types so that the signals seen in Figure 4 can be properly interpreted.

3.2. Hygroscopicity

One would expect that the seasonal and latitudinal gradient of CCN is related to the CCN type in nature, and chemical composition is an intrinsic quality for analysis. However, few observations about chemical composition are available from MARCUS and even the closest associated variable is just an indirect reflection of aerosol chemical composition. Hygroscopicity is a fundamental aerosol property that describes the tendency of an aerosol to absorb water vapor from the ambient environment in order to grow and controls the propensity of a particle to act as a CCN. A widely used parameter to quantify hygroscopicity is the aerosol particle size Hygroscopic Growth Factor (HGF), which is defined here as the ratio of the wet particle diameter at Relative Humidity (RH) of 80% to the corresponding dry diameter. A higher HGF means that an aerosol is more capable of absorbing water.

The HTDMA used during MARCUS was set at a specific sample flow of 0.8 L per minute. Measurements made during dry relative humidity (RH) (wet RH is always set at 80%) larger than 20% and ship stack contamination have been removed. Figure 5 shows a plot of different size aerosols' HGF measured by the HTDMA, colored based on whether data were collected over the NSO or SSO. Over the NSO, the HGF mostly increases as aerosol size increases, from a minimum HGF mode near 1.4 for 150 nm to a maximum mode near 1.7 for 250 nm particles. This increase with particle size indicates that larger particles are more capable of absorbing water vapor over the NSO. Over the SSO, the HGF has two modes for 50 nm particles, but in general one consistent mode for larger particles which falls within the range of 1.4–1.6. The spread of HGF is larger as the dry size of the aerosols increases.

There were no aerosol mass spectrometers used during MARCUS. Thus, aerosol composition is assessed using the HGF data under the context of measurements obtained in previous campaigns. Previous studies (e.g., Xu et al., 2020) have assumed some mixture of commonly occurring chemicals for marine aerosols, consisting of organic matter, non-sea-salt sulfate, nitrate, ammonium, sea salt and black carbon. Various mixing rules are applied to predict aerosol hygroscopicity. However, the inverse problem of determining composition from hygroscopic measurements is much more challenging.

Asmi et al. (2010) measured the hygroscopicity of summertime sub-100 nm aerosols off the Antarctic coast at the Aboa station using an impactor for the size-segregated composition of marine aerosol particles, reporting that the measured HGF at 90% RH was 1.71 for 90 nm particles. MARCUS data show a mode of 1.4 and 1.6 for 100 nm particles over the NSO and SSO respectively, both smaller than these previous measurements. But MARCUS HTDMA measurements were made at an RH of 80% so exact agreement would not be expected.

Another relevant comparison with previous studies is that of the HGF derived hygroscopicity parameter kappa κ (Petters & Kreidenweis, 2007). For the reason that the CCN measurements acquired during MARCUS were not dried upstream of the CCN inlet while the UHSAS measurements were dried as a protocol for size measurement, assumptions of dry particles in Petters and Kreidenweis (2007) used to derive κ with paired CCN-UHSAS data are

Figure 4. Latitudinal dependence of N_{CCN} and N_{Ac} (within one degree bin) and its seasonal components. Subplot (a) is for the whole MARCUS period, while subplot (b) is for November and December, and (d) for January and February. Shadows fill in ranges between the 1st and 3rd quartile. The number of 10-min samples measured in each latitude degree bin is shown in (c) for November and December, and in (e) for January and February. The CCN measured at supersaturation 0.2% and 0.5% are plotted in blue and red respectively, with points representing mean and lines connecting the median. The black points and lines stand for mean and median number concentration of Ac measured by the UHSAS. The green lines with dots show the ratio between $N_{CCN,0.2}$ and $N_{CCN,0.5}$ in (c) and (e).

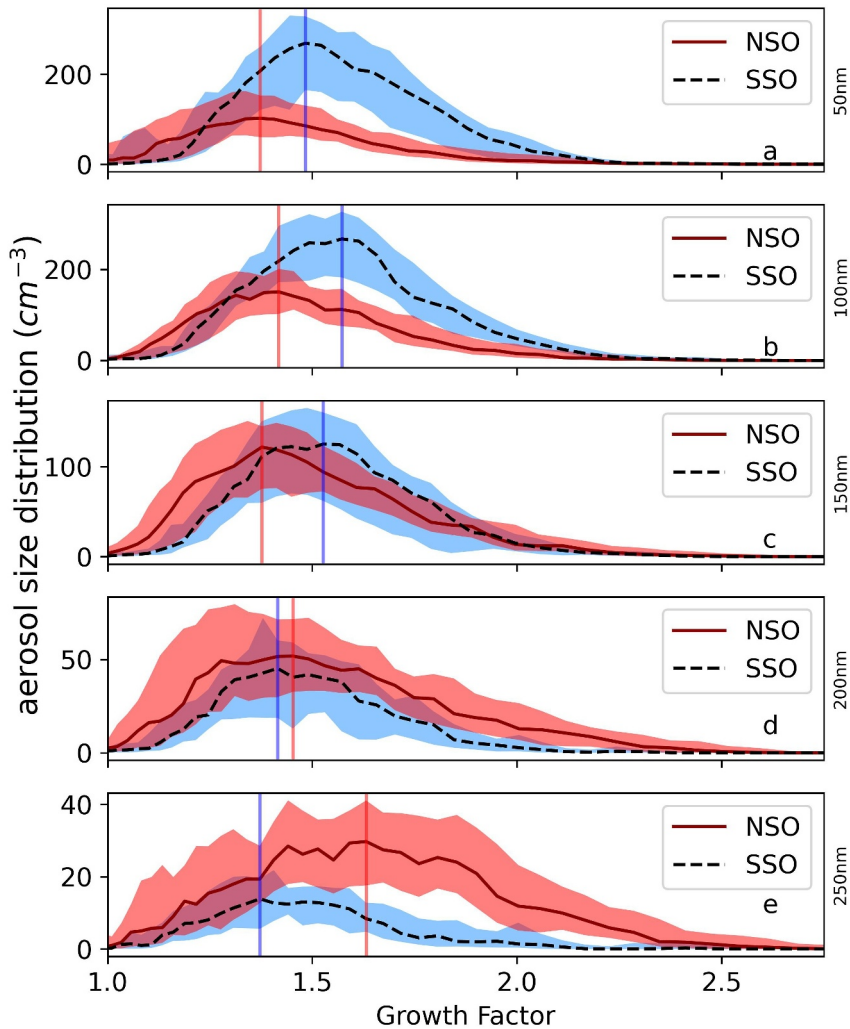

Figure 5. Aerosol number concentration divided by log scale bin width versus hygroscopic Growth Factor at 80% RH for particle sizes (50, 100, 150, 200, and 250 nm from a to e) from the HTDMA. Red color and blue color represent NSO and SSO, respectively, the solid lines and dotted lines plot the median within each bin and shadings cover the range between the first and the third quartile in each bin. The red vertical line is the mode for the 3rd quartile of HGF over the NSO and the blue line for the SSO.

not satisfied here. Future experiments over the SO should dry particles measured by both the CCN and UHSAS to minimize the influences from solid water coating and ice crystals which may occur when the ship is close to the sea ice and snow, considering Gong et al. (2023) showed blowing snow can be a good source for CCN over the sea ice in polar area. However, the HTDMA measurements mostly satisfy the assumptions in Petters and Kreidenweis (2007) and the HGF derived κ is shown in Figure S9 of the Supporting Information S1. Based on reference values (κ of $(NH_4)_2SO_4$, Na_2SO_4 and organics), the derived κ over both NSO and SSO have size dependence, indicating heterogeneous composition across sizes. To compare with the CCN-derived κs from previous study, Tatzelt et al. (2022) mentioned that CCN showed variable contributions of organic and inorganic material (inter-quartile range of hygroscopicity parameter κ from 0.2 to 0.9), which is consistent with Figure S9 in this study of the Supporting Information S1. The derived κ for particles with 250 nm dry diameter over the NSO is close to the κ of sulfate ($(NH_4)_2SO_4$, Na_2SO_4). And the κ over the SSO have unique peak values close to the κ of sulpate ($(NH_4)_2SO_4$, Na_2SO_4) for particles with 100 nm dry diameter.

Climate models and laboratory experiments report HGF and κ assuming an aerosol is composed of a single ingredient. Natural aerosols, however, can be a mix of various chemical compositions. Several hypotheses can be thus formulated. The small value of HGF over the NSO of 1.4 suggests a potential composition of organic

aerosols, which have a HGF close to 1.2–1.4. The mode of 1.6 over the SSO is consistent with the contribution from MSA which has a HGF close to 1.6, or/and the contribution from sulfate which has a HGF of 1.7–1.8. The MSA could be dimethyl-sulfide emitted from the ocean surface from the oxidation of phytoplankton byproducts, and the organic aerosols could be associated with the oxidation of volatile organic compounds emitted from the wind-wave interactions. The longer tail present as the dry diameter increases is hypothesized to be related to the increased composition of sea salt over the NSO whose HGF can be as large as 2.3 for 90 nm particles. The sea salt aerosols are likely sea sprays from the higher surface winds over the NSO (Humphries et al., 2021). The first mode of the HGF for 50 nm particles over the SSO is consistent with the presence of iodine which has a HGF of 1.1 and can contribute to polar particle formation processes (Murray et al., 2012).

To summarize Sections 3.1 and 3.2, the hypotheses about the chemical compositions from the HTDMA consistent with the observations implies there may be more primary CCN over the NSO and more secondary CCN over the SSO. The distinct hygroscopicity of aerosols and their corresponding sources may be one of the reasons for the different cloud properties over the NSO and SSO. Further, the SSO has higher number concentration of small particles as shown in Figures 5a and 5b (blue peaks higher than red peaks), while the NSO has a greater population of larger particles as shown in Figures 5d and 5e. Examination of the Angstrom exponent in Section 4 offers more insight into these differences. Future measurements over the SO should include information on the chemical composition so as to better relate the aerosol species and the HGF distributions. An examination of the aerosol size distribution may also help interpret the observed increases of N_{CCN} over the SSO.

3.3. Accumulation Mode Aerosols

To further look into the causes of the observed N_{CCN} gradient, the variation of CCN size with season and latitude over the NSO and SSO was investigated. To do this the accumulation mode aerosols (Ac) size distribution measured by the UHSAS are analyzed in this section.

Figure 6 shows the latitudinal dependence of N_{Ac} during the entire time of MARCUS (Figure 6a), and for the spring (Figure 6b) and summer (Figure 6d) separately. The Ac concentration from small (70 nm < D < 100 nm) and large (700 nm < D < 1,000 nm) particles, respectively hereafter smaller Ac and larger Ac, derived from the UHSAS size distribution are also shown. Over the SO, on average 67% of the N_{Ac} is contributed by the smaller Ac with only an average of 2% from larger Ac. As shown in Figure 6a, the median line in red shows that overall larger Ac have concentrations >2 cm^{-3} over the NSO and stay below 2 cm^{-3} over the SSO. The larger aerosols have lower concentrations over the SSO in both spring and summer. As discussed in Section 1, the larger Ac are likely primarily sea spray aerosols, and the increased concentrations over the NSO are likely the result of higher surface wind speeds over the NSO (Moore et al., 2022; Sanchez et al., 2021). Wind speed measurements acquired from the AA show that the mode of the surface wind speed was 10–15 ms^{-1} over the NSO and 5–10 ms^{-1} over the SSO. The sea ice present over parts of the SSO can also contribute to the low number concentration of larger Ac.

The latitudinal dependence of the total Ac concentration is similar to that of N_{70-100}, which is not surprising given smaller particles dominate the total Ac. Another way to show the relative difference in concentrations between the larger Ac and smaller Ac is the ratio between $N_{CCN,0.2}$ and $N_{CCN,0.5}$ (Figures 4c and 4e). During the spring, both latitude bins centered at 58°S and 59°S in Figure 6b show a large gap between total Ac and N_{70-100}, indicating fractions of Ac with $D > 100$ nm as large as 75% and 73%, with large Ac mean concentrations of $N_{700-1000}$ of 3.5 and 3.7 cm^{-3}. The production of large aerosols at these locations can be related to the impact of the higher average surface wind speeds, 10.7 and 9.9 ms^{-1} respectively measured at 58°S and 59°S during the spring. Similar large gaps between Ac and small Ac show up at 51°S and 54°S during the spring, both have coincident high values of large Ac and surface winds. During the spring, small Ac contributes to a larger fraction of Ac over the SSO than over the NSO. In general, over the NSO, there is a higher fraction of small particles contributing to total Ac in the summer than in the spring. Further, over the summer SSO, this fraction is less than 40% between 64°S and 66°S.

3.4. Angstrom Exponent

For the sub-micron aerosols over the SO, while the small Ac ($N_{70-100nm}$) can be more related to the secondary organic aerosols and associated RPF events, the large Ac ($N_{700-1000nm}$) can be the results of wind-wave interaction and should be better illustrated by optical properties since the optical cross section and not the total number concentration determines the extinction. Figure 7 shows the normalized frequency distribution of scattering α over the NSO and SSO for aerosols with D < 1,000 nm that were measured by the nephelometer. There are higher

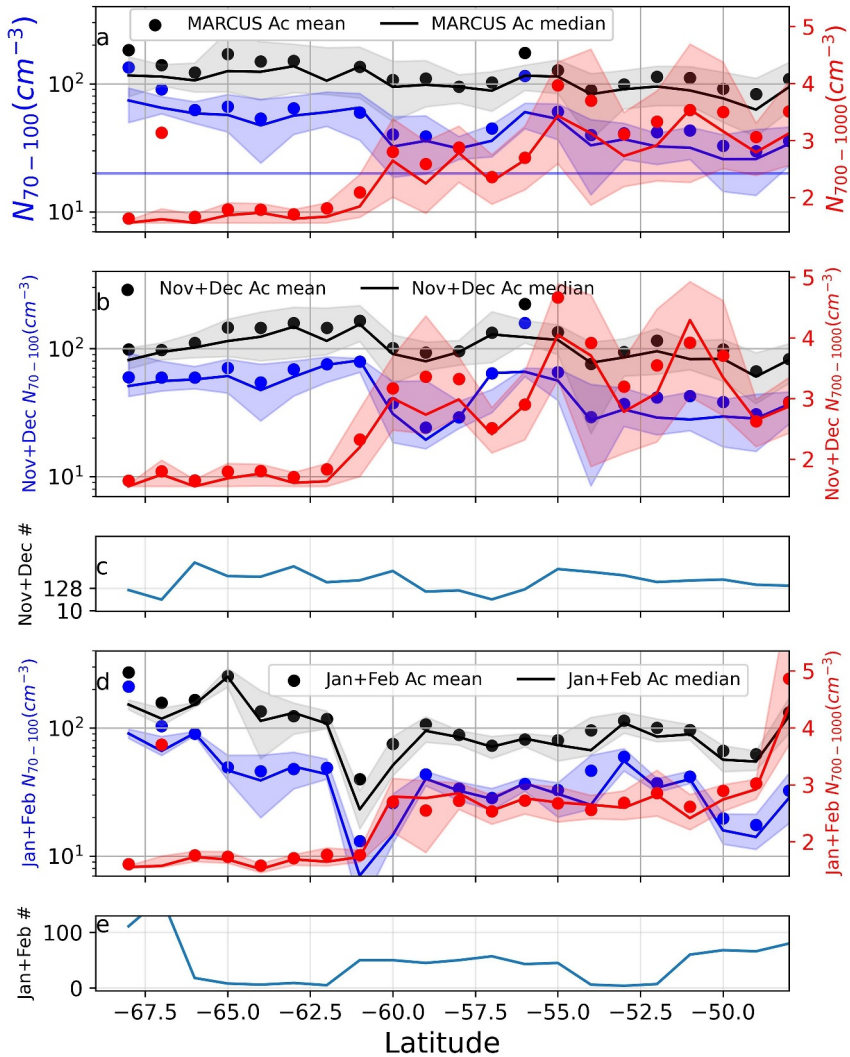

Figure 6. Latitudinal dependence of N_{Ac}, $N_{70-100nm}$, and $N_{700-1000nm}$ in black (log scale), blue (log scale), and red (linear scale, ticks on the right) in different seasons. Subplot (a) is for the whole MARCUS period, while subplot (b and d) are respectively for spring (November and December), and summer (January and February). Points represent median and lines connect the means. Shadows fill in ranges between the 1st and 3rd quartile. The number of samples measured in each latitude degree bin in spring and summer are displayed in subplot (c) and (e).

α modes over the SSO for all the pairs of wavelengths with a mode of 1.1 for α measured between 450 and 550 nm wavelength ($\alpha_{450-550nm}$), 1.4 for α measured between 450 and 700 nm wavelength ($\alpha_{450-700}$), and 1.5 for α measured between 550 and 700 nm wavelength ($\alpha_{550-700}$). There are lower α modes over the NSO, with 0.5 for $\alpha_{450-550nm}$, 0.8 for $\alpha_{450-700}$ and 1.0 for $\alpha_{550-700}$. The differences of α between the SSO and NSO are significant at the 0.05 level. This shows atmospheric aerosols acquired over the SSO consist of relatively smaller particles and those over the NSO consist of relatively larger particles in the sub-micron size range. This is consistent with the analysis of aerosol size distributions shown in Figures 4 and 6.

The decreased values of α compared to those closer to the Antarctic can be explained by more sea spray PM_1 over the NSO and more recent formed PM_1 over the SSO (Humphries et al., 2021; I. L. McCoy et al., 2021; Sanchez et al., 2021). From the perspective of potential physical processes, this is consistent with the distribution of coastal sea ice affecting sea spray production under wind stress (Humphries et al., 2021; Twohy et al., 2021), the sedimentation and/or rain-out of large aerosols during long range transport of pollution over the NSO (Humphries et al., 2016, 2021; Sanchez et al., 2021), and the varied contributions between primary and secondary aerosol formation including RPF between the NSO and SSO (Humphries et al., 2021; Sanchez et al., 2021).

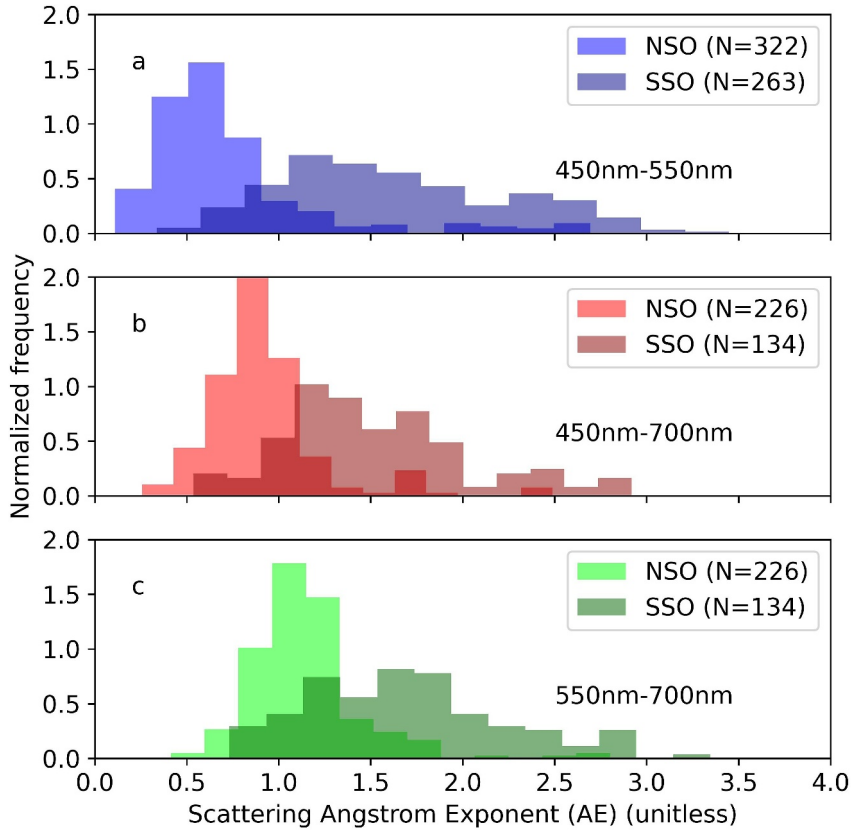

Figure 7. Sub-micron SO aerosol scattering Angstrom Exponent (AE) normalized density distribution derived from the Nephelometer in the latitude range between 50 and 60°S and the latitude range south of the 62°S. Sub-panels (a) through (c) represent AE derived with different pair of wavelengths, as shown in each figure by text under the legend.

Due to the lack of instruments covering the complete range of aerosols in the measured size distributions, a complete size distribution is not available, particularly for aerosols with D < 60 nm and D > 1,000 nm, no conclusion can be made directly about the modes of aerosol sizes outside of the measurement range of the UHSAS. However, measured optical properties as a function of wavelength can be used to deduce aerosol size modes over the full range of sizes. For example, over both the SSO and NSO, α increases with wavelength, but the rate of increase is different. Instead of using the linear relation between λ and the natural logarithm of AOD given by Equation 2, Eck et al. (2001) developed a more precise empirical fit between AOD and wavelength, given by

$$\ln Bs(\lambda) = \alpha_0 + \alpha_1 ln\lambda + \alpha_2 (\ln \lambda)^2, \tag{4}$$

where

$$\alpha'(\lambda) = \frac{d\alpha}{dln\lambda} = -2\alpha_1. \tag{5}$$

The derived α' according to Equation 5 is 2.24 over the NSO and 1.80 over the SSO. Both values are positive, implying a negative curvature (convex of α with λ), which corresponds to a dominance of fine mode aerosols (Barman et al., 2019; Soni et al., 2011). This confirms that fine mode consistent with prior studies (D < 200 nm) aerosols are dominant over both the NSO and SSO, with the effective radius over the SSO being smaller than that over the NSO given the smaller α. This is consistent with the measured size distributions and number concentrations shown in Figure 6.

Based on various aerosol production mechanisms active over the remote oceans, the chemical composition of a primary marine aerosol is closely related to its size. For example, the over-micron aerosols and larger Ac can

originate from the sea spray, while the smaller Ac and Aitken mode aerosols can originate from processes related to recent particle formation events and cloud droplet residues, and thus contain sulfate. This correlation between aerosol size and chemical composition derived over the complete possible range of aerosol sizes has been confirmed by Humphries et al. (2021).

3.5. Primary and Secondary Aerosols

In summary, over the NSO, the higher surface wind speeds can be related to more primary CCN. Humphries et al. (2021) showed greater precipitation over the NSO, which can be related to heavier wet-scavenging (collision-coalescence of an aerosol and a water droplet) for both primary and secondary CCN and thus a lower N_{CCN} compared to the SSO. The Ac is also larger by size over the NSO (Figures 4 and 7) which can be more hygroscopic (Figure 4). This can be related to a greater nucleation scavenging efficiency (CCN inducing formation of cloud droplets in supersaturated water vapor) and thus lower N_{CCN} given similar meteorological conditions. Thus there can be both greater production and greater loss of larger Ac over the NSO, and the production of primary CCN can be greater than that over the SSO based on the size distribution. Over the SSO, there exists greater sea ice coverage and less surface wind speeds. However the greater production of secondary CCN can overweigh the less production of primary CCN over the SSO, particularly during the summer months. This overweight together with a less wet-removal (wet scavenging and nucleation removal) efficiency caused by smaller particle sizes can be related to a higher N_{CCN} over the SSO.

Moore et al. (2024) inferred that the marine boundary layer INPs, at least during Austral summer, are dominated by particles with D < 500 nm. If the above-mentioned discernible latitudinal variation of N_{CCN} between NSO and SSO is related to the shift from more primary CCN over the NSO to more secondary CCN over the SSO, the patterns of INPs are also worthwhile to investigate from a seasonal and latitudinal perspective.

4. Ice Nucleating Particles

Given the low values of N_{INP} over the SO (McCluskey, Hill, Humphries, et al., 2018; Welti et al., 2020), open-faced filters were collected over a period of 23–48hr during MARCUS in order to acquire enough total INP for different treatments. The presence of sea ice over the SSO made the ship speed over the SSO slower than over the NSO, meaning higher numbers of INP samples were collected over the SSO compared to over the NSO for the same range of latitudes given comparable sample collection times. Nevertheless, sometimes the lower N_{INP} over the SSO strongly challenges the Ice Spectrometer lowest detection limit, particularly during the offline treatments to identify INP types.

Figure 8 shows the latitudinal dependence of the N_{INP}-temperature spectra over the NSO and SSO. On average, N_{INP} over the SSO is less than that over the NSO, particularly that between 50°S and 55°S. This trend is consistent with observations shown in Kremser et al. (2021) during the 2018 February–March field campaign across the SO, from Wellington, New Zealand, to the Ross Sea, Antarctica. The latitudinal dependence of N_{INP} over the NSO is more significant than that over the SSO. At a temperature of −25°C, the standard deviation of N_{INP} sampled over the NSO is twice than that over the SSO. This may imply that there are different or more INP sources present across the latitudes over the NSO than over the SSO for the period of this study. After heating to 95°, heat-labile INPs such as those of biological origin are removed. Figure 8b compared with Figure 8a illustrates heat-labile proteinaceous INP may be more prevalent at higher latitudes (in darker red) consistent with increased biology activities. There is also an increase of N_{INP} after the heating of a few of the northern samples, which is consistent with a restructuring of organic coatings or fragmentation of entities such as gels or bacteria that contain INPs/IN activity. Figure 8e shows those N_{INP} that have the greatest reduction in concentration after the heating treatment, as noted especially by the lowering of concentrations at temperatures greater than −23°C, were acquired close to the Antarctic coast. This is consistent with cold carbon-rich, high nutrient up-welling close to the Antarctic coastal area, or the marginal ice zone, providing heat-labile and presumably proteinacious INPs. It is also possible that land sources of biological INPs emanate from the Antarctic itself. The exact source remains to be determined. The treatment of H_2O_2 digestion and heating ensures the remaining refractory INPs are non-organic, primarily dust (McCluskey, Hill, Humphries, et al., 2018). Figure 8c shows the latitudinal dependence of the refractory non-organic INPs' is not strong, while Figure 8f shows that the concentration of these refractory INPs is higher when closer to the Antarctic coast (except for the 68.57°S sample). These results indicate that the majority of INPs observed at all latitudes during MARCUS had biological or organic influences greater than the influences of in-organics.

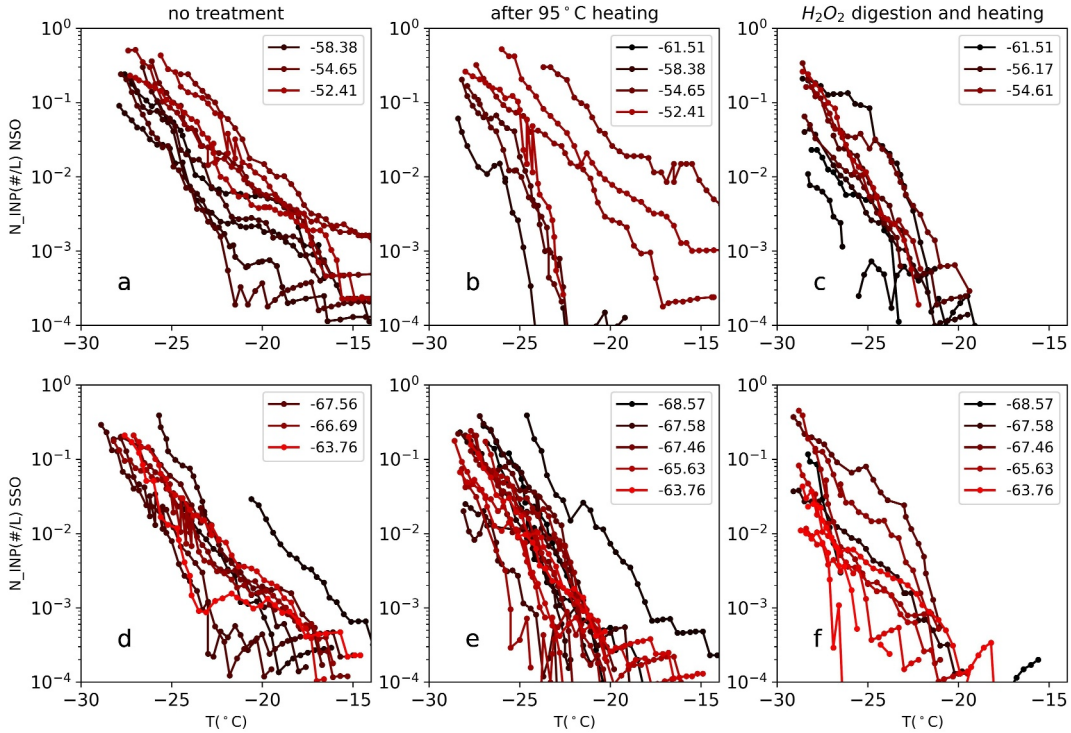

Figure 8. Latitudinal dependence of untreated (a and d), heated (b and e), and refractory (c and f) N_{INP} temperature spectra over the NSO (the first row) and SSO (the second row). The legend labels show the latitude in unit of south degrees, with the black lines representing observations acquired closer to the Antarctic and the red ones closer to Australia. Legends are shown every four lines.

Figure 9 shows the seasonal transition of N_{INP} over the NSO and SSO. Generally, the seasonal dependence is stronger over the NSO (Figure 9a) than over the SSO (Figure 9d). Over the NSO, Figure 9a shows INPs measured in November and December have lower concentrations than those in February and March, which passes the significance test at a 0.01 level given −23°C as a reference temperature. These February and March NSO INPs also have greater concentrations than SSO INPs in general, which is consistent with the presence of more sea spray INPs over the NSO. The SSO INPs have less seasonal variability according to Figure 9d. One explanation of this trend is that the more biologically active SSO releases biogenic INPs during the entire summer and spring, whereas the biological activity over the NSO varies by season. Further, the NSO releases more sea spray INPs into the atmosphere given less sea ice cover and higher surface wind speeds. The NSO also has closer proximity to transport from larger open land regions. Figure 9b shows that N_{INP} in November and December are most sensitive to heating for temperature increases above −24°C, indicating the deactivation of ice-nucleating-active-proteins. Differences between the left and middle columns illustrate the contribution from biological INPs. The samples collected during March have higher N_{INP} and are mostly heat-stable, indicating the increased INPs in the NSO in later summer are coming from organic INP primarily, but not necessarily biological INPs. Most of the March samples were collected during the cruise between Hobart and Macquarie island, where wind speeds were higher, suggesting more sea salt INPs would have been released into the atmosphere. Figure 9e shows biogenic N_{INP} over the SSO have limited seasonal variation in the spring and summer. Figure 9c shows a stronger seasonal dependence of refractory N_{INP} after digestion and heating treatment, which is mostly dust, over the NSO compared to that over the SSO shown in Figure 9f. This might be influenced by dust transportation considering the samples collected during the Macquarie island voyage are closer to open land regions and prone to dust events. But in general, the derived ratio between non-biogenic INPs and all INPs varies between 0.01 and 0.3 at −25°C, implying that most INPs are biogenic in origin, whether from the sea or from land. Even if the organics are determined to be attached to dust, the organics are dominating ice nucleation.

Using airborne data collected over the SO, Twohy et al. (2021) showed that the top three components of the airborne sampled INP composition (active from −27 to −32°C) over the NSO were organic, crustal/metals, and

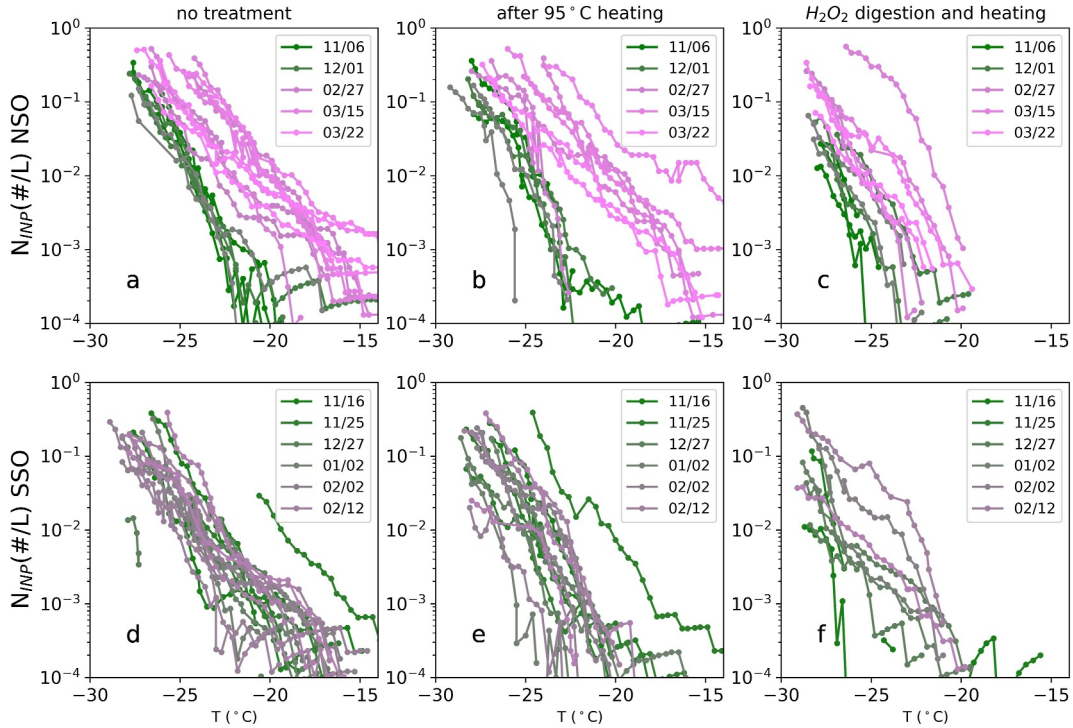

Figure 9. Seasonal dependence of untreated (a and d), heated (b and e), and refractory (c and f) N_{INP} temperature spectra over the NSO and SSO respectively in the first and second row. The legend labels show the dates in 2017 and 2018. Legends are shown every four lines.

sea spray with high sulfur content, with mean fractions of 0.35, 0.26, and 0.23 respectively. From the combined analysis of Figures 9 and 8, the following conclusions on the presence of INPs over the SO are reached. Results from peroxide digestion and heat treatment show that the spring and summertime organics are mostly active at temperatures higher than −20°C. At this temperature range, most INPs are biogenic in origin, even if attached to dust, with organics dominating. Specifically, INPs acquired during March had the highest number concentration, probably from the contribution of sea spray-produced INPs.

5. Summary and Discussion

Measurements of maritime surface aerosols acquired during MARCUS using in situ aerosol probes on the RSV Aurora Australis (AA) as it traversed over the Southern Ocean provide an opportunity to investigate the latitudinal and seasonal variations of CN, CCN, and INPs over the SO. Within the pristine boundary layer far from both anthropogenic emissions and continental sources, sea spray aerosols, normally regarded as primary aerosols, including sea salts and biological proteinaceous aerosols, that can be effective CCN and INPs, are present. In addition, sulfur-based secondary aerosols with smaller sizes can contribute to the CCN over the SO. The principal conclusions from this study are summarized as follows:

(1) Higher CCN concentrations were observed over the SSO than over the NSO, with increased numbers of $N_{CCN,0.5}$ over the SSO given SO typical supersaturations between 0.3% and 0.4%.
(2) The different aerosol compositions hypothesized to be present over the SO are consistent with observations of Hygroscopicity Growth Factor from the HTDMA, which provides an indirect measurement of CCN chemical composition. It indicates that 50–250 nm accumulation mode aerosols over both the SSO and NSO have different hygroscopicity growth factors (HGFs) which depend on size. The HGF over the NSO mostly increases as size increases, consistent with a change in composition dominated by organic aerosols to one dominated by sulfates, or/and affected by sea salt composition. The HGFs over the SSO are less sensitive to dry diameter changes, with the values of HGFs derived hygroscopicity parameter κ close to the κ of sulfates for particles with dry diameter of 250 nm.

(3) Size shifting happened between the NSO and SSO. Accumulation mode aerosols have larger concentrations for larger sizes over the NSO compared to the SSO as derived from both the measured optical properties and size distributions. In particular, though both the NSO and SSO have limited $N_{700-1000nm}$ that are enhanced under conditions of high surface winds, the SSO has $N_{700-1000nm}$ as low as $<cm^{-3}$, and the NSO $N_{700-1000nm}$ ranges from 2 to 5 cm^{-3} depending on latitude. Over the SSO, there are substantial concentrations of Aitken mode and small accumulation mode aerosols compared to further north. One would suspect that biogenic emissions from the summertime Antarctic coast together with the following gas phase oxidation, and growth to the accumulation mode could cause these trends.

(4) From the latitudinal perspective, the INPs over the SSO had lower concentrations than over the NSO, but greater fractions of biological INPs, particularly during January and February, as indicated by the concentration of INPs after a heating treatment.

(5) The seasonal variation of INPs is larger than the latitudinal variation, particularly over the NSO, with summertime concentrations being up to 10 times larger than those in early spring for a −25°C reference temperature. The heating treatment and organic carbon digestion treatment of the INP suspensions prior to immersion freezing testing reveals that INPs originate from primarily organic and biological sources. The seasonal dependence of INPs over the NSO is stronger than over the SSO and could be associated with a seasonal shifting of biological proteins and organics from wind-wave interactions.

Based on the conclusions above, one would expect the large seasonal and latitudinal variation of N_{CCN} is related to small sulfur-based aerosols being effective CCN. However, no chemical compositions were measured during MARCUS to confirm this. Such measurements should be an important component for future field campaigns in this area. Although the HTDMA data give indirect inferences about chemistry, blowing snow, particularly over the SSO, may affect the data quality. Future studies should also examine meteorological controls of aerosol concentration and properties, in addition to the seasonal and latitudinal dependence, in order to better quantify processes responsible for the observed patterns of CN, CCN, and INPs over the SO. Further studies should also conduct local high-resolution simulations of aerosols over the SO to better understand the sources and sinks of aerosols, including their transport, aggregation, coagulation, and dry and wet scavenging. This will ultimately help quantify aerosol-clouds interactions in the pristine marine boundary layer.

Data Availability Statement

Data sets utilized in this study are all publicly available from the Department of Energy Atmospheric Radiation Measurement Data Discovery https://adc.arm.gov/discovery/#/results/s::marcus%20aerosol. Citations including DOIs or URLs for individual data sets are provided at relevant locations within the paper. Quality controlled aerosols data after ship stack contamination removal used in this study can be found in Niu (2024), https://doi.org/10.5281/zenodo.10792712.

Acknowledgments
The efforts of the entire MARCUS team in collecting the high-quality data used in this study are appreciated. Technical, logistical, and ship support for MARCUS were provided by the Australian Antarctic Division through Australian Antarctic Science Projects 4431, 4292, and 4387. QN, GMM, and RM acknowledge support from the United States Department of Energy (US DOE) through Grants DE-SC0018626 and DE-SC0021159. CSM was supported through US DOE grant DE-SC0020098. RM was also supported through DE-SC0016225. RH was supported in this project by funding the Australian Government and by BER Award DESC0018995. PJD and TCJH acknowledge support from the US DOE through Grant DE-SC0021116. This material is based upon work supported by the National Center for Atmospheric Research, which is a major facility sponsored by the National Science Foundation under Cooperative Agreement No. 1852977. This study is facilitated by OU Supercomputing Center for Education and Research. We also acknowledge Markus Petters for figure interpretation, and Ashish Singh, Janek Uin, Rebecca Trojanowski, Jessie Creamean, and Olga L. Mayol-Bracero for their help on instrument uncertainties.

References

Ångström, A. (1929). On the atmospheric transmission of sun radiation and on dust in the air. *Geografiska Annaler*, *11*(2), 156–166. https://doi.org/10.1080/20014422.1929.11880498

Asmi, E., Frey, A., Virkkula, A., Ehn, M., Manninen, H. E., Timonen, H., et al. (2010). Hygroscopicity and chemical composition of Antarctic sub-micrometre aerosol particles and observations of new particle formation. *Atmospheric Chemistry and Physics*, *10*(9), 4253–4271. https://doi.org/10.5194/acp-10-4253-2010

Assessment, A. M. S. (2009). Report. *Arctic Council*.

Barman, N., Saha, B., Roy, R., Kundu, S., Borgohain, A., & Raju, P. (2019). Investigation of curvature effect of Ångström exponent to classify the aerosol types over the region of interest (88°–98°E and 20°–30°N). *Atmospheric Pollution Research*, *10*(2), 363–373. https://doi.org/10.1016/j.apr.2018.09.002

Bodas-Salcedo, A., Hill, P. G., Furtado, K., Williams, K. D., Field, P. R., Manners, J. C., et al. (2016). Large contribution of supercooled liquid clouds to the solar radiation budget of the Southern Ocean. *Journal of Climate*, *29*(11), 4213–4228. https://doi.org/10.1175/JCLI-D-15-0564.1

Bodas-Salcedo, A., Williams, K. D., Ringer, M. A., Beau, I., Cole, J. N. S., Dufresne, J.-L., et al. (2014). Origins of the solar radiation biases over the Southern Ocean in CFMIP2 models. *Journal of Climate*, *27*(1), 41–56. https://doi.org/10.1175/JCLI-D-13-00169.1

Brooks, S. D., & Thornton, D. C. (2018). Marine aerosols and clouds. *Annual Review of Marine Science*, *10*(1), 289–313. https://doi.org/10.1146/annurev-marine-121916-063148

Burrows, S. M., Hoose, C., Pöschl, U., & Lawrence, M. G. (2013). Ice nuclei in marine air: Biogenic particles or dust? *Atmospheric Chemistry and Physics*, *13*(1), 245–267. https://doi.org/10.5194/acp-13-245-2013

D'Alessandro, J. J., McFarquhar, G. M., Wu, W., Stith, J. L., Jensen, J. B., & Rauber, R. M. (2021). Characterizing the occurrence and spatial heterogeneity of liquid, ice, and mixed phase low-level clouds over the Southern Ocean using in situ observations acquired during SOCRATES. *Journal of Geophysical Research: Atmospheres*, *126*(11), e2020JD034482. https://doi.org/10.1029/2020JD034482

DeMott, P., Hill, T., & McFarquhar, G. (2018). Measurements of aerosols, radiation, and clouds over the Southern Ocean (MARCUS). Ice Nucleating Particle Measurements Field Campaign Report. *12*.

Eck, T. F., Holben, B. N., Ward, D. E., Dubovik, O., Reid, J. S., Smirnov, A., et al. (2001). Characterization of the optical properties of biomass burning aerosols in Zambia during the 1997 ZIBBEE field campaign. *Journal of Geophysical Research*, *106*(D4), 3425–3448. https://doi.org/10.1029/2000JD900555

Fawcett, T. (2006). An introduction to ROC analysis. *Pattern Recognition Letters*, *27*(8), 861–874. https://doi.org/10.1016/j.patrec.2005.10.010

Flato, G., Marotzke, J., Abiodun, B., Braconnot, P., Chou, S. C., Collins, W., et al. (2013). Evaluation of climate models. In T. F. Stocker, et al. (Eds.), *Climate change 2013: The physical science basis. Contribution of working group I to the fifth assessment report of the intergovernmental panel on climate change* (pp. 741–882). Cambridge University Press. https://doi.org/10.1017/CBO9781107415324.020

Fossum, K., Ovadnevaite, J., Ceburnis, D., Dall´osto, M., Marullo, S., Bellacicco, M., et al. (2018). Summertime primary and secondary contributions to Southern Ocean cloud condensation nuclei. *Scientific Reports*, *8*(1), 13844. https://doi.org/10.1038/s41598-018-32047-4

Gettelman, A., Bardeen, C. G., McCluskey, C. S., Järvinen, E., Stith, J., Bretherton, C., et al. (2020). Simulating observations of Southern Ocean clouds and implications for climate. *Journal of Geophysical Research: Atmospheres*, *125*(21), e2020JD032619. https://doi.org/10.1029/2020JD032619

Gong, X., Zhang, J., Croft, B., Yang, X., Frey, M. M., Bergner, N., et al. (2023). Arctic warming by abundant fine sea salt aerosols from blowing snow. *Nature Geoscience*, *16*(9), 768–774. https://doi.org/10.1038/s41561-023-01254-8

Gras, J. (1995). CN, CCN and particle size in Southern Ocean air at cape grim. *Atmospheric Research*, *35*(2), 233–251. https://doi.org/10.1016/0169-8095(94)00021-5

Hamilton, D. S., Lee, L. A., Pringle, K. J., Reddington, C. L., Spracklen, D. V., & Carslaw, K. S. (2014). Occurrence of pristine aerosol environments on a polluted planet. *Proceedings of the National Academy of Sciences of the United States of America*, *111*(52), 18466–18471. https://doi.org/10.1073/pnas.1415440111

Hoose, C., Kristjánsson, J. E., Iversen, T., Kirkevåg, A., Seland, O., & Gettelman, A. (2009). Constraining cloud droplet number concentration in GCMs suppresses the aerosol indirect effect. *Geophysical Research Letters*, *36*(12), L12807. https://doi.org/10.1029/2009GL038568

Hoskins, B. J., & Hodges, K. I. (2005). A new perspective on southern hemisphere storm tracks. *Journal of Climate*, *18*(20), 4108–4129. https://doi.org/10.1175/JCLI3570.1

Hu, X.-M., Xue, M., Kong, F., & Zhang, H. (2019). Meteorological conditions during an ozone episode in Dallas-Fort Worth, Texas, and impact of their modeling uncertainties on air quality prediction. *Journal of Geophysical Research: Atmospheres*, *124*(4), 1941–1961. https://doi.org/10.1029/2018JD029791

Hu, Y., Rodier, S., Xu, K.-M., Sun, W., Huang, J., Lin, B., et al. (2010). Occurrence, liquid water content, and fraction of supercooled water clouds from combined CALIOP/IIR/MODIS measurements. *Journal of Geophysical Research*, *115*(D4), D00H34. https://doi.org/10.1029/2009JD012384

Huang, Y., Protat, A., Siems, S. T., & Manton, M. J. (2015). A-train observations of maritime midlatitude storm-track cloud systems: Comparing the Southern Ocean against the North Atlantic. *Journal of Climate*, *28*(5), 1920–1939. https://doi.org/10.1175/JCLI-D-14-00169.1

Huang, Y., Siems, S. T., Manton, M. J., Hande, L. B., & Haynes, J. M. (2012). The structure of low-altitude clouds over the Southern Ocean as seen by cloudsat. *Journal of Climate*, *25*(7), 2535–2546. https://doi.org/10.1175/JCLI-D-11-00131.1

Huang, Y., Siems, S. T., Manton, M. J., Protat, A., & Delanoë, J. (2012). A study on the low-altitude clouds over the Southern Ocean using the DARDAR-MASK. *Journal of Geophysical Research*, *117*(D18), D18204. https://doi.org/10.1029/2012JD017800

Humphries, R. S., Keywood, M. D., Gribben, S., McRobert, I. M., Ward, J. P., Selleck, P., et al. (2021). Southern ocean latitudinal gradients of cloud condensation nuclei. *Atmospheric Chemistry and Physics Discussions*, *2021*, 1–35. https://doi.org/10.5194/acp-2020-1246

Humphries, R. S., Klekociuk, A. R., Schofield, R., Keywood, M., Ward, J., & Wilson, S. R. (2016). Unexpectedly high ultrafine aerosol concentrations above East Antarctic sea ice. *Atmospheric Chemistry and Physics*, *16*(4), 2185–2206. https://doi.org/10.5194/acp-16-2185-2016

Humphries, R. S., McRobert, I. M., Ponsonby, W. A., Ward, J. P., Keywood, M. D., Loh, Z. M., et al. (2019). Identification of platform exhaust on the RV *Investigator*. *Atmospheric Measurement Techniques*, *12*(6), 3019–3038. https://doi.org/10.5194/amt-12-3019-2019

Humphries, R. S., Schofield, R., Keywood, M. D., Ward, J., Pierce, J. R., Gionfriddo, C. M., et al. (2015). Boundary layer new particle formation over East Antarctic sea ice—Possible Hg-driven nucleation? *Atmospheric Chemistry and Physics*, *15*(23), 13339–13364. https://doi.org/10.5194/acp-15-13339-2015

IPCC. (2013). *Climate change 2013: The physical science basis. contribution of working group I to the fifth assessment report of the intergovernmental panel on climate change*. Cambridge University Press. https://doi.org/10.1017/CBO9781107415324

Kang, L., Marchand, R., & Smith, W. (2021). Evaluation of MODIS and Himawari-8 low clouds retrievals over the Southern Ocean with in situ measurements from the SOCRATES campaign. *Earth and Space Science*, *8*(3), e2020EA001397. https://doi.org/10.1029/2020EA001397

Kaufman, Y. J. (1993). Aerosol optical thickness and atmospheric path radiance. *Journal of Geophysical Research*, *98*(D2), 2677–2692. https://doi.org/10.1029/92JD02427

Koontz, A., Flynn, C., Shilling, J., & Flynn, C. (2018). Aerosol optical properties (aoppsap1flynn1m). https://doi.org/10.5439/1369240

Koontz, A., Kuang, C., Andrews, E., Hayes, C., Singh, A., & Salwen, C. (2018). Condensation particle counter (aoscpcf). https://doi.org/10.5439/1352536

Kremser, S., Harvey, M., Kuma, P., Hartery, S., Saint-Macary, A., McGregor, J., et al. (2021). Southern ocean cloud and aerosol data: A compilation of measurements from the 2018 Southern Ocean Ross Sea marine ecosystems and environment voyage. *Earth System Science Data*, *13*(7), 3115–3153. https://doi.org/10.5194/essd-13-3115-2021

Kuang, C. (2016a). Condensation particle counter instrument handbook. https://doi.org/10.2172/1245983

Kuang, C. (2016b). TSI model 3936 scanning mobility particle spectrometer instrument handbook. https://doi.org/10.2172/1245993

Lang, F., Huang, Y., Siems, S. T., & Manton, M. J. (2018). Characteristics of the marine atmospheric boundary layer over the Southern Ocean in response to the synoptic forcing. *Journal of Geophysical Research: Atmospheres*, *123*(15), 7799–7820. https://doi.org/10.1029/2018JD028700

Mace, G. G. (2010). Cloud properties and radiative forcing over the maritime storm tracks of the Southern Ocean and North Atlantic derived from a-train. *Journal of Geophysical Research*, *115*(D10), D10201. https://doi.org/10.1029/2009JD012517

Mace, G. G., Benson, S., Humphries, R., Gombert, P. M., & Sterner, E. (2023). Natural marine cloud brightening in the Southern Ocean. *Atmospheric Chemistry and Physics*, *23*(2), 1677–1685. https://doi.org/10.5194/acp-23-1677-2023

Mallet, M. D., Humphries, R. S., Fiddes, S. L., Alexander, S. P., Altieri, K., Angot, H., et al. (2023). Untangling the influence of Antarctic and Southern Ocean life on clouds. *Elementa: Science of the Anthropocene*, *11*(1), 00130. https://doi.org/10.1525/elementa.2022.00130

McCluskey, C. S., Hill, T. C. J., Humphries, R. S., Rauker, A. M., Moreau, S., Strutton, P. G., et al. (2018). Observations of ice nucleating particles over Southern Ocean waters. *Geophysical Research Letters*, *45*(21), 11989–11997. https://doi.org/10.1029/2018GL079981

McCluskey, C. S., Hill, T. C. J., Sultana, C. M., Laskina, O., Trueblood, J., Santander, M. V., et al. (2018). A mesocosm double feature: Insights into the chemical makeup of marine ice nucleating particles. *Journal of the Atmospheric Sciences*, *75*(7), 2405–2423. https://doi.org/10.1175/JAS-D-17-0155.1

McCoy, D. T., Burrows, S. M., Wood, R., Grosvenor, D. P., Elliott, S. M., Ma, P.-L., et al. (2015). Natural aerosols explain seasonal and spatial patterns of Southern Ocean cloud albedo. *Science Advances*, *1*(6). https://doi.org/10.1126/sciadv.1500157

McCoy, D. T., Hartmann, D. L., & Grosvenor, D. P. (2014). Observed Southern Ocean cloud properties and shortwave reflection. Part II: Phase changes and low cloud feedback. *Journal of Climate*, *27*(23), 8858–8868. https://doi.org/10.1175/JCLI-D-14-00288.1

McCoy, I., McCoy, D., Wood, R., Regayre, L., Watson-Parris, D., Grosvenor, D., et al. (2020). The hemispheric contrast in cloud microphysical properties constrains aerosol forcing. *Proceedings of the National Academy of Sciences of the United States of America*, *117*(32), 18998–19006. https://doi.org/10.1073/pnas.1922502117

McCoy, I. L., Bretherton, C. S., Wood, R., Twohy, C. H., Gettelman, A., Bardeen, C. G., & Toohey, D. W. (2021). Influences of recent particle formation on Southern Ocean aerosol variability and low cloud properties. *Journal of Geophysical Research: Atmospheres*, *126*(8), e2020JD033529. https://doi.org/10.1029/2020JD033529

McFarquhar, G. M., Bretherton, C., Marchand, R., Protat, A., DeMott, P. J., Alexander, S. P., et al. (2021). Observations of clouds, aerosols, precipitation, and surface radiation over the Southern Ocean: An overview of CAPRICORN, MARCUS, MICRE and SOCRATES. *Bulletin of the American Meteorological Society*, *102*(4), 1–92. https://doi.org/10.1175/BAMS-D-20-0132.1

Moore, K. A., Alexander, S. P., Humphries, R. S., Jensen, J., Protat, A., Reeves, J. M., et al. (2022). Estimation of sea spray aerosol surface area over the Southern Ocean using scattering measurements. *Journal of Geophysical Research: Atmospheres*, *127*(22), e2022JD037009. https://doi.org/10.1029/2022JD037009

Moore, K. A., Hill, T. C. J., McCluskey, C. S., Twohy, C. H., Rainwater, B., Toohey, D. W., et al. (2024). Characterizing ice nucleating particles over the Southern Ocean using simultaneous aircraft and ship observations. *Journal of Geophysical Research: Atmospheres*, *129*(2), e2023JD039543. https://doi.org/10.1029/2023JD039543

Murray, B. J., Haddrell, A. E., Peppe, S., Davies, J. F., Reid, J. P., O'Sullivan, D., et al. (2012). Glass formation and unusual hygroscopic growth of iodic acid solution droplets with relevance for iodine mediated particle formation in the marine boundary layer. *Atmospheric Chemistry and Physics*, *12*(18), 8575–8587. https://doi.org/10.5194/acp-12-8575-2012

Naud, C. M., Booth, J. F., & Del Genio, A. D. (2014). Evaluation of ERA-interim and MERRA cloudiness in the Southern Ocean. *Journal of Climate*, *27*(5), 2109–2124. https://doi.org/10.1175/JCLI-D-13-00432.1

Niu, Q. (2024). Supporting information of JGR-A paper supporting information 2024 [Dataset]. *Zenodo*. https://doi.org/10.5281/zenodo.10792712

Pedregosa, F., Varoquaux, G., Gramfort, A., Michel, V., Thirion, B., Grisel, O., et al. (2011). Scikit-learn: Machine learning in python. *Journal of Machine Learning Research*, *12*(85), 2825–2830. Retrieved from http://jmlr.org/papers/v12/pedregosa11a.html

Petters, M. D., & Kreidenweis, S. M. (2007). A single parameter representation of hygroscopic growth and cloud condensation nucleus activity. *Atmospheric Chemistry and Physics*, *7*(8), 1961–1971. https://doi.org/10.5194/acp-7-1961-2007

Quinn, P. K., Coffman, D. J., Kapustin, V. N., Bates, T. S., & Covert, D. S. (1998). Aerosol optical properties in the marine boundary layer during the first aerosol characterization experiment (ace 1) and the underlying chemical and physical aerosol properties. *Journal of Geophysical Research*, *103*(D13), 16547–16563. https://doi.org/10.1029/97JD02345

Raman, A., Hill, T., DeMott, P. J., Singh, B., Zhang, K., Ma, P.-L., et al. (2023). Long-term variability in immersion-mode marine ice-nucleating particles from climate model simulations and observations. *Atmospheric Chemistry and Physics*, *23*(10), 5735–5762. https://doi.org/10.5194/acp-23-5735-2023

Sanchez, K. J., Roberts, G. C., Saliba, G., Russell, L. M., Twohy, C., Reeves, J. M., et al. (2021). Measurement report: Cloud processes and the transport of biological emissions affect Southern Ocean particle and cloud condensation nuclei concentrations. *Atmospheric Chemistry and Physics*, *21*(5), 3427–3446. https://doi.org/10.5194/acp-21-3427-2021

Schmale, J., Baccarini, A., Thurnherr, I., Henning, S., Efraim, A., Regayre, L., et al. (2019). Overview of the Antarctic circumnavigation expedition: Study of preindustrial-like aerosols and their climate effects (ace-space). *Bulletin of the American Meteorological Society*, *100*(11), 2260–2283. https://doi.org/10.1175/BAMS-D-18-0187.1

Schuster, G. L., Dubovik, O., & Holben, B. N. (2006). Angstrom exponent and bimodal aerosol size distributions. *Journal of Geophysical Research*, *111*(D7), D07207. https://doi.org/10.1029/2005JD006328

Simmonds, I., & Keay, K. (2000). Mean southern hemisphere extratropical cyclone behavior in the 40-year NCEP–NCAR reanalysis. *Journal of Climate*, *13*(5), 873–885. https://doi.org/10.1175/1520-0442(2000)013⟨0873:MSHECB⟩2.0.CO;2

Sinha, P., Hobbs, P., Yokelson, R., Bertschi, I., Blake, D., Simpson, I., et al. (2003). Emissions of trace gases and particles from savanna fires in southern Africa. *Journal of Geophysical Research*, *108*(D13), 8487. https://doi.org/10.1029/2002JD002325

Soni, K., Singh, S., Bano, T., Tanwar, R. S., & Nath, S. (2011). Wavelength dependence of the aerosol angstrom exponent and its implications over Delhi, India. *Aerosol Science and Technology*, *45*(12), 1488–1498. https://doi.org/10.1080/02786826.2011.601774

Sun, Z., & Shine, K. (1994). Studies of the radiative properties of ice and mixed-phase clouds. *Quarterly Journal of the Royal Meteorological Society*, *120*(515), 111–137. https://doi.org/10.1002/qj.49712051508

Tang, G., Liu, Y., Zhang, J., Liu, B., Li, Q., Sun, J., et al. (2021). Bypassing the NOx titration trap in ozone pollution control in Beijing. *Atmospheric Research*, *249*, 105333. https://doi.org/10.1016/j.atmosres.2020.105333

Tatzelt, C., Henning, S., Welti, A., Baccarini, A., Hartmann, M., Gysel-Beer, M., et al. (2022). Circum-Antarctic abundance and properties of CCN and INPS. *Atmospheric Chemistry and Physics*, *22*(14), 9721–9745. https://doi.org/10.5194/acp-22-9721-2022

Turner, D. R., Hassellöv, I.-M., Ytreberg, E., & Rutgersson, A. (2017). Shipping and the environment: Smokestack emissions, scrubbers and unregulated oceanic consequences. *Elementa: Science of the Anthropocene*, *5*. https://doi.org/10.1525/elementa.167

Twohy, C. H., DeMott, P. J., Russell, L. M., Toohey, D. W., Rainwater, B., Geiss, R., et al. (2021). Cloud-nucleating particles over the Southern Ocean in a changing climate. *Earth's Future*, *9*(3), e2020EF001673. https://doi.org/10.1029/2020EF001673

Uetake, J., Hill, T. C. J., Moore, K. A., DeMott, P. J., Protat, A., & Kreidenweis, S. M. (2020). Airborne bacteria confirm the pristine nature of the Southern Ocean boundary layer. *Proceedings of the National Academy of Sciences of the United States of America*, *117*(24), 13275–13282. https://doi.org/10.1073/pnas.2000134117

Uin, J. (2016d). 3002 humidified tandem differential mobility analyzer instrument handbook. https://doi.org/10.2172/1251403

Uin, J. (2016a). Cloud condensation nuclei particle counter (CCN) instrument handbook. https://doi.org/10.2172/1251411

Uin, J. (2016b). Integrating nephelometer instrument handbook. https://doi.org/10.2172/1246075

Uin, J. (2016c). Ultra-high-sensitivity aerosol spectrometer (UHSAS) instrument handbook. https://doi.org/10.2172/1251410

Uin, J., Aiken, A. C., Dubey, M. K., Kuang, C., Pekour, M., Salwen, C., et al. (2019). Atmospheric radiation measurement (ARM) aerosol observing systems (AOS) for surface-based in situ atmospheric aerosol and trace gas measurements. *Journal of Atmospheric and Oceanic Technology*, *36*(12), 2429–2447. https://doi.org/10.1175/JTECH-D-19-0077.1

Uin, J., Andrews, E., Enekwizu, O., Hayes, C., & Salwen, C. (2018). Cloud condensation nuclei particle counter (aosccn1colspectra). https://doi.org/10.5439/1342134

Uin, J., Cromwel, E., Hayes, C., & Salwen, C. (2018). Humidified tandem differential mobility analyzer (aoshtdma). https://doi.org/10.5439/1095581

Uin, J., Salwen, C., Senum, G., & Hayes, C. (2018). Nephelometer (aosnephdry1m). https://doi.org/10.5439/1984586

Uin, J., Senum, G., Koontz, A., Flynn, C., Salwen, C., & Hayes, C. (2018). Ultra-high sensitivity aerosol spectrometer (aosuhsas). https://doi.org/10.5439/1409033

Uin, J., & Smith, S. (2020). ARM AOS. https://www.arm.gov/capabilities/instruments/aos

Welti, A., Bigg, E. K., DeMott, P. J., Gong, X., Hartmann, M., Harvey, M., et al. (2020). Ship-based measurements of ice nuclei concentrations over the Arctic, Atlantic, Pacific and Southern Oceans. *Atmospheric Chemistry and Physics*, *20*(23), 15191–15206. https://doi.org/10.5194/acp-20-15191-2020

Williams, J., de Reus, M., Krejci, R., Fischer, H., & Ström, J. (2002). Application of the variability-size relationship to atmospheric aerosol studies: Estimating aerosol lifetimes and ages. *Atmospheric Chemistry and Physics*, *2*(2), 133–145. https://doi.org/10.5194/acp-2-133-2002

Xi, B., Dong, X., Zheng, X., & Wu, P. (2022). Cloud phase and macrophysical properties over the Southern Ocean during the MARCUS field campaign. *Atmospheric Measurement Techniques*, *15*(12), 3761–3777. https://doi.org/10.5194/amt-15-3761-2022

Xu, W., Ovadnevaite, J., Fossum, K. N., Lin, C., Huang, R.-J., O'Dowd, C., & Ceburnis, D. (2020). Aerosol hygroscopicity and its link to chemical composition in the coastal atmosphere of mace head: Marine and continental air masses. *Atmospheric Chemistry and Physics*, *20*(6), 3777–3791. https://doi.org/10.5194/acp-20-3777-2020

Zhou, X., Atlas, R., McCoy, I. L., Bretherton, C. S., Bardeen, C., Gettelman, A., et al. (2021). Evaluation of cloud and precipitation simulations in CAM6 and AM4 using observations over the Southern Ocean. *Earth and Space Science*, *8*(2), e2020EA001241. https://doi.org/10.1029/2020EA001241